Heliyon 6 (2020) e05329

Contents lists available at ScienceDirect

Heliyon

journal homepage: www.cell.com/heliyon

Research article

# Synthesis opto-electronic characterization and NLO evaluation of 6-methyl 5-nitro Uracil crystal using XRD, spectroscopic and theoretical tools

K. Sooryakala [a,b], S. Ramalingam [b,*], R. Maheswari [a], R. Aarthi [c]

[a] Department of Physics, S.T.E.T. Women's College[1], Sundarakkottai, Mannargudi, Tamilnadu, India
[b] Department of Physics, A.V.C. College(Autonomous)[1], Mayiladuthurai, Tamilnadu, India
[c] Department of Physics, ST. Theresa's Arts and Science College for Women[1], Tharangambadi, Tamilnadu, India

ARTICLE INFO

*Keywords:*
Materials science
Materials chemistry
6-Methyl 5-nitro Uracil
NLO activity
Orthorhombic lattice
NBMO
Dichroic image

ABSTRACT

The organic composite crystal for 6-methyl 5-nitro Uracil was grown using slow-evaporation method and the crystal quality was checked by observing the peaks in XRD pattern. The molecular structure of 6-methyl 5-nitro Uracil was used to find crystal parameters for determining NLO activity. The appropriate electronic geometrical structure was keenly noted and the transitional energy exchange was studied and thereby fine-tuning of crystal performance was made by adopting suitable electron-accepting and with-drawing substitutional groups. The crystal parameters; a≠b≠c confirmed the orthorhombic lattice pattern. The space group was found as $P_{21/a}$ and Transparency range was observed as 409–1256 nm. The laser measurements were made and laser Damage threshold was estimated at 10 ns[1.08–3 GW/cm$^2$]. The scattering characteristics of bond networks over the molecule were observed by studying vibrational characteristics of elemental bonds. The hybrid calculations on DFT methods were made using B3LYP/6-311++(D,P) basis set. The chemical shift was observed and retracing chemical potential was identified from the parametric oscillation. The frontier molecular interactions between ground and excited orbital lobe overlapping segments were noted and type of interaction system was identified. The electronic and protonic transfer energy was measured and the origination point of equivalent chemical potential was acknowledged. The NBMO profile was keenly grafted and the transitional energy was measured at every consumed electronic energy band. The vibrational circular dichroic image for all vibrational regions was sketched and the rate of transmission and absorption ratio was verified from peak intensity.

## 1. Introduction

For the past decades, beyond technological boundaries, the crystal engineering field of research is being developed due to their ultimate needs in the electronic and optical industry. Nowadays, by the application of modern scientific developments, new and novel electro-optical and nonlinear optical materials in the form of high dense crystalline semiconductor solids have been developed and it is the promising materials and able to replace all the inorganic materials like silicon and associated metallic solid constituents [1]. Predominantly, organically made crystalline semiconductors are having great attention in the field of NLO communication and optical controlled electronic devices fabrication due to their easy customization of required property and fine-tuning of material applications. The organic synthesize and evaluation of properties are easy and viable in present days because of NLO material modeling, simple and feasible mode of synthesis of crystals, prompt evaluation by readily available tools and utilization of crystalline semiconductors possessed preferable functions by adopting customization of fascinating topological architectures [2].

In such a way, the Uracil is a trendy organic species that having ultimate crystal property (such as the physico-chemical property can be tuned by adopting suitable ligands with it) to induce moderate NLO activity [3, 4]. In micro-electronic engineering standpoint, Uracil derivative crystals are very fascinating in the field of NLO branch of research since their ability to stimulate the NLO mechanism by adopting σ-σ* and π-π*stacking interaction and Sp, Sp$^2$ hybridization interactive overlapping systems that offered by endo-cyclic-double bond nitrogen and exo-cyclic-double bond oxygen quasi-centers [5, 6]. After investigating the literatures [7, 8, 9, 10, 11, 12, 13, 14], it was found that, no novel organic complex crystal has been grown with electronic and optical

* Corresponding author.
*E-mail address:* ramalingam.physics@gmail.com (S. Ramalingam).
[1] All institutions are affiliated to Bharathidasan University, Truchirappalli, Tamilndu, India.

https://doi.org/10.1016/j.heliyon.2020.e05329
Received 20 April 2020; Received in revised form 19 May 2020; Accepted 20 October 2020

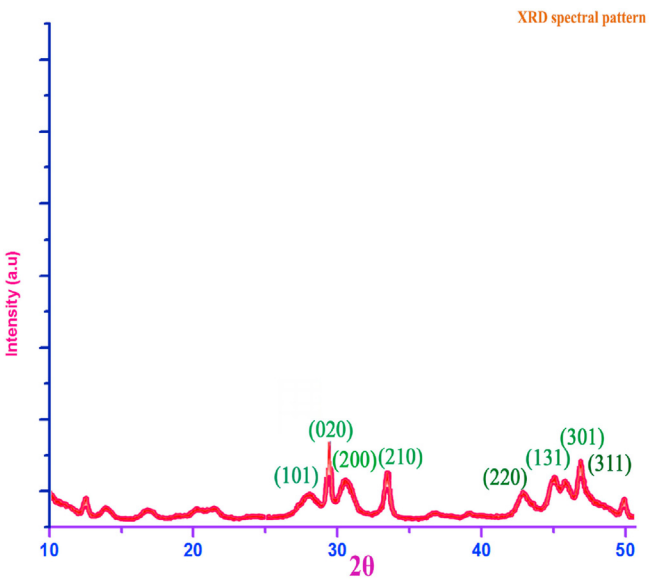


**Figure 1.** XRD pattern of 6-methyl 5-nitro Uracil crystal.

properties. In a similar way, the injection of methyl group enabling (lone pair) LP-σ interaction entities and nitro group substitution facilitate additional π-π* interaction and thereby the enriched low HOMO-LUMO interactive systems [15, 16]. Therefore, it is necessary to investigate all the crystallographic, dielectric, physical, and chemical properties to be evaluated by growing crystal; 6-methyl 5-nitro Uracil for determining NLO activity and optical controlled opto-electronic process for fabricating novel ultra-high frequency optical communication devices. By screening available literature, there were seemed to be no work established on organic crystal growth on title compound to evaluate the NLO ability. The present work was carried out to synthesize the crystal, characterize morphologically to evaluate the crystal lattice using molecular spectroscopy, and computational calculations and validate the NLO property.

## 2. Experimental details

### 2.1. Crystal preparation

The raw solid-phase 6-methyl 5-nitro Uracil was mixed with DMSO solution and stirred well with a magnetic stirrer and the solution was allowed to enter into thick-walled quartz ampoules at the bottom of the furnace. Then, the ampoules were perfectly evacuated ($<10^{-4}$ Torr) and sealed completely. In the growth process, heating was carried out at the rate from 15 to 25° C/hour which is the opt rate of the present material. The vertical furnace of the set up was switched on thereby the density of resistance wire was heated up. Thus, the single crystal in the vessel was grown up from a 6-methyl 5-nitro Uracil seed at the bottom. The temperature about 215 °C at the furnace was maintained and the seed was saturated at such temperature around 10 h and slowly cold down to room temperature and finally the single crystal was grown. The fabricated crystal was cleaned and made cleavage as required.

### 2.2. Recording of XRD and molecular spectra

The chemical specimen was purchased from Sigma Aldrich Company USA which was found to be pure and high spectroscopic grade. The XRD pattern was recorded for a raw sample of the present case and the clear XRD pattern was determined for the analysis. The FT-IR spectral pattern

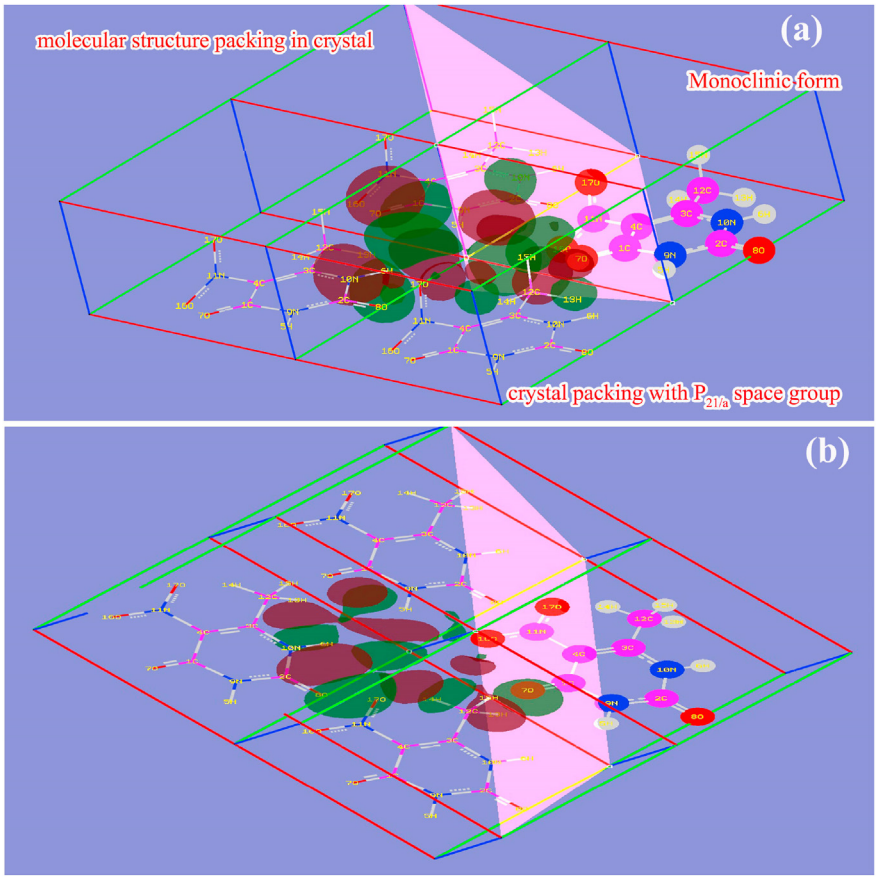


**Figure 2.** (a) monoclinic (b) (111) view of Molecule in crystal view of 6-methyl 5-nitro Uracil.

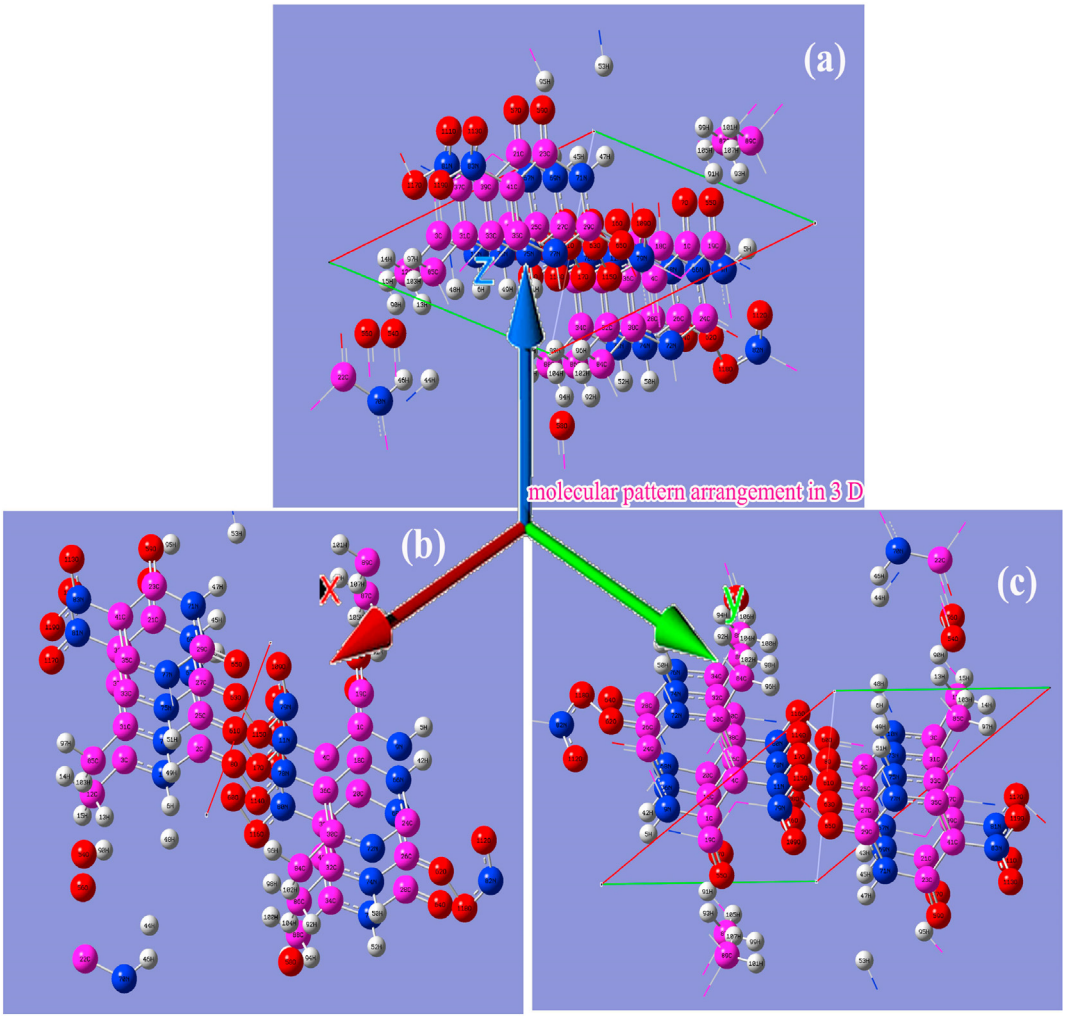


**Figure 3.** (a) x view (b)y view (c) z view for Optical pathway mechanism of 6-methyl 5-nitro Uracil crystal.

was sequentially recorded using a Bruker IFS 66V with high-resolution spectrometer after making several scanning processes for getting the good results. The FT-Raman spectral wavenumbers were recorded using Bruker spectrometer adopted with an FT-IR instrument with Raman module equipped with a Nd: YAG laser source being operated at 1.063 μm line width with 400 mW power. The high resolution $^{1}$H NMR and $^{13}$C NMR spectra were recorded using 600 MHz and 55 MHz NMR spectrometers with high magnetic resolution. The UV-Visible spectral pattern was recorded in the region of 50 nm–800 nm, with the scanning interval of 0.50 nm, using the UV-1800 series instrument. The crystalline transmission spectra were also acquired from the same apparatus and being allowed to produce polarization for an optical beam.

**Table 1.** Crystal evaluation data of 6-methyl 5-nitro Uracil.

| Crystal parameters | Constants |
|---|---|
| Crystal constant | |
| a | 4.75Å |
| b | 7.10Å |
| c | 7.39Å |
| α | 89.8° |
| β | 81.41° |
| γ | 86.69° |
| Crystal lattice type | Orthorhombic |
| Space group | $P_{21/a}$ |
| Refractive index | $N_x = 1.586$; $N_y = 1.963$; $N_z = 1.739$; at $\lambda = 509$ nm |
| Birefringence Δn | 0.2106 |
| Transparency range | 409–1256 nm |
| Non-Linear optical coefficient | 7.82 pm/V |
| Damage threshold | 10 ns[1.08–3 GW/cm$^2$] |
| Properties | Good air conservation |

### 2.3. Laser measurements

The refractive index measurement was made by two crystalline prisms, in that, the bisector planes contain two dielectric axes in which one was along the zenith. For optical measurements, three refractive indices were estimated by the minimal deviation method. The laser measurements were carried out using Nd.YAG continuous at 1.06 μm. The birefringence patterns and phase matching peaks for the present compounds were obtained by Q-switched Nd:YAG laser discharging 10 ns pulses at 1.064 μm at a 20-Hz reiteration rate. For the present case, laser Damage-threshold measurements were performed at a 10-Hz successive rate with 10-ns pulse duration.

## 3. Computational methods

The molecular structure was optimized by making a stability scan using RIC system at various coordinate systems by using suitable hybrid DFT methods such as B3LYP/6-311++G(2d,p) and all the calculations

**Table 2.** Molecular/crystal parameters of 6-methyl 5-nitro uracil.

| Parameters | Values |
|---|---|
| Hydrogen bond donor count | 2 |
| Hydrogen bond acceptor count | 4 |
| Rotatable bond count | 0 |
| Topological Polar Surface Area | 104A$^2$ |
| Molecular mass and MW | 171.11 g/mol |
| Heavy Atom Count | 12 |
| Log p | -0.57 |
| N atoms | 12 |
| n ON | 7 |
| n OHNH | 2 |
| n violations | 0 |
| nrotb | 1 |
| Molecular Volume | 131.88 |

have been performed in iMac computer. All the structural and vibrational bond parameters were calculated using B3LYP/6-311++G(2d,2p) and are made to coincide with experimental values by error reducing methods. The UV-Visible transmission and absorption spectra and their parameters were calculated by performing computations using the method of B3LYP/6-311++G(2d,2p) with an energy profile. The $^{13}$C and $^{1}$H NMR chemical parametric values are computed and tabulated and also spectrograph was recorded according to TMS specimen values.

## 4. Results and discussions

### 4.1. XRD measurement analysis

The XRD peaks were obtained from different planes of grown crystal and are displayed in Figure 1. As the crystal is grown by the optimal method, the effective peaks observed on (020) plane, (101), and (131) plane, (200), (210) and (220) plane and (301) and (311) planes, respectively, at 28°, 28°, 29°, 32, 34, 43°, 45°, 46° and 50°. These peaks showed in second -order y plane, first-order x & z plane, second-order XY planes and third-order X and Y planes in that order. Such observation of peaks ensured the viable growing efficiency in XYZ planes. Some of the other peaks were suppressed in different planes which explicit the limitation zones of XYZ planes. All the signals from different planes emphasize the orthorhombic crystal lattice model of the grown crystal. The peak intensity was moderate and that was due to the controlled growing efficacy of the normal free grow methods and the process of method was not complicated for NLO crystal using organic composite.

As the Uracil crystal was most rigid due to the strong binding nature of the hexagonal frame adopted with $NO_2$, $CH_3$ and = O groups. All these groups naturally supported the ring for the molecular arrangement in the crystal structure. The hybrid crystal packing is shown in Figure 2 where

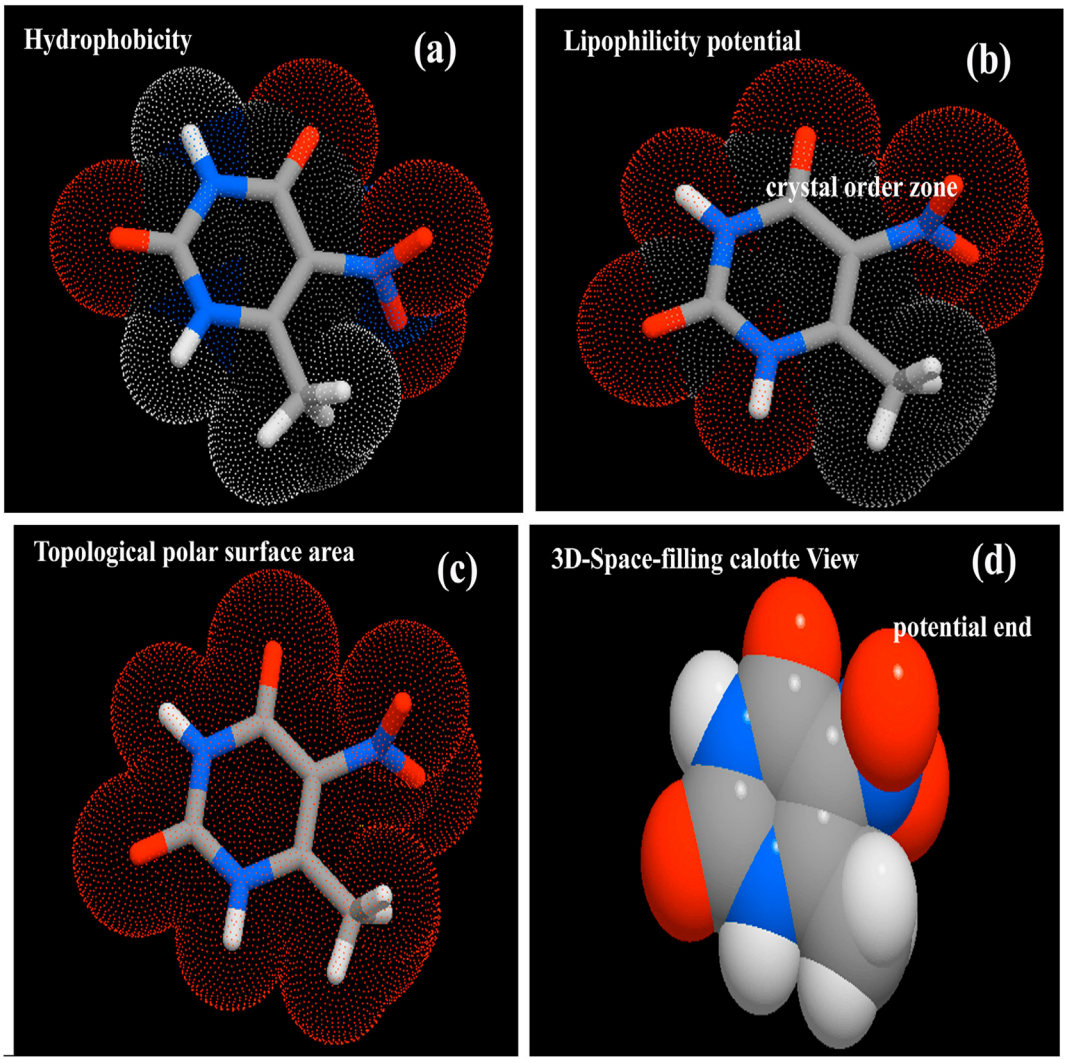


**Figure 4.** (a) Hydrophobicity (b) Lipophilicity (c) TPSA (d) 3D space filling profile of 6-methyl 5-nitro Uracil crystal.

**Table 3.** Optimized geometrical parameters for6-methyl 5-nitro Uracil computed at different methods.

| Geometrical Parameters | Methods | | | |
|---|---|---|---|---|
| | HF | B3LYP | | B3PW91 |
| | 6-311+G (d, p) | 6-31++G (d, p) | 6-311++G (d, p) | 6-311+G (d, p) |
| **Bond length (Å)** | | | | |
| C1–C4 | 1.467 | 1.470 | 1.468 | 1.465 |
| C1–O7 | 1.183 | 1.215 | 1.208 | 1.206 |
| C1–N9 | 1.388 | 1.409 | 1.409 | 1.404 |
| C2–O8 | 1.186 | 1.217 | 1.209 | 1.207 |
| C2–N9 | 1.365 | 1.378 | 1.379 | 1.374 |
| C2–N10 | 1.380 | 1.399 | 1.399 | 1.394 |
| C3–C4 | 1.341 | 1.368 | 1.362 | 1.361 |
| C3–N10 | 1.366 | 1.372 | 1.372 | 1.367 |
| C3–C12 | 1.502 | 1.502 | 1.500 | 1.494 |
| C4–N11 | 1.453 | 1.456 | 1.462 | 1.455 |
| H5–N9 | 0.998 | 1.014 | 1.013 | 1.012 |
| H6–N10 | 0.995 | 1.012 | 1.011 | 1.010 |
| N11–O16 | 1.180 | 1.226 | 1.218 | 1.213 |
| N11–O17 | 1.193 | 1.238 | 1.230 | 1.224 |
| C12–H13 | 1.084 | 1.094 | 1.092 | 1.093 |
| C12–H14 | 1.077 | 1.090 | 1.087 | 1.088 |
| C12–H15 | 1.085 | 1.095 | 1.094 | 1.094 |
| **Bond angle ()** | | | | |
| C4–C1–O7 | 126.20 | 126.92 | 126.87 | 126.87 |
| C4–C1–N9 | 112.79 | 112.66 | 112.47 | 112.43 |
| O7–C1–N9 | 120.98 | 120.38 | 120.63 | 120.67 |
| O8–C2–N9 | 124.11 | 124.80 | 124.84 | 124.84 |
| O8–C2–N10 | 122.15 | 122.07 | 122.26 | 122.27 |
| N9–C2–N10 | 113.74 | 113.12 | 112.91 | 112.89 |
| C4–C3–N10 | 118.51 | 118.25 | 118.34 | 118.34 |
| C4–C3–C12 | 126.76 | 126.30 | 126.30 | 126.23 |
| N10–C3–C12 | 114.73 | 115.45 | 115.36 | 115.44 |
| C1–C4–C3 | 122.05 | 122.19 | 122.37 | 122.29 |
| C1–C4–N11 | 117.42 | 117.78 | 117.54 | 117.66 |
| C3–C4–N11 | 120.52 | 120.03 | 120.10 | 120.05 |
| C1–N9–C2 | 127.60 | 128.00 | 128.16 | 128.30 |
| C1–N9–H5 | 116.18 | 115.78 | 115.73 | 115.68 |
| C2–N9–H5 | 116.17 | 116.19 | 116.09 | 116.01 |
| C2–N10–C3 | 125.26 | 125.73 | 125.72 | 125.73 |
| C2–N10–H6 | 114.84 | 114.30 | 114.45 | 114.45 |
| C3–N10–H6 | 119.89 | 119.96 | 119.82 | 119.82 |
| C4–N11–O16 | 117.32 | 117.43 | 117.25 | 117.14 |
| C4–N11–O17 | 117.34 | 117.47 | 117.44 | 117.38 |
| O16–N11–O17 | 125.34 | 125.10 | 125.31 | 125.47 |
| C3–C12–H13 | 109.38 | 110.27 | 110.12 | 110.19 |
| C3–C12–H14 | 112.11 | 111.74 | 111.97 | 111.97 |
| C3–C12–H15 | 108.84 | 109.71 | 109.57 | 109.52 |
| H13–C12–H14 | 109.45 | 109.17 | 109.22 | 109.22 |
| H13–C12–H15 | 108.91 | 108.88 | 108.69 | 108.71 |
| H14–C12–H15 | 108.08 | 106.98 | 107.18 | 107.13 |
| **Dihedral angles ()** | | | | |
| O7–C1–C4–C3 | 175.45 | 175.70 | 175.95 | 175.96 |
| O7–C1–C4–N11 | -3.50 | -4.12 | -3.81 | -3.83 |
| N9–C1–C4–C3 | -2.69 | -2.24 | -2.10 | -2.08 |
| N9–C1–C4–N11 | 178.37 | 177.94 | 178.15 | 178.13 |
| C4–C1–N9–C2 | 2.19 | 1.39 | 1.27 | 1.22 |
| C4–C1–N9–H5 | 179.53 | 179.50 | 179.47 | 179.43 |
| O7–C1–N9–C2 | -176.06 | -176.70 | -176.91 | -176.95 |
| O7–C1–N9–H5 | 1.28 | 1.41 | 1.28 | 1.26 |
| O8–C2–N9–C1 | 179.10 | 179.62 | 179.64 | 179.67 |

(*continued on next page*)

**Table 3** (*continued*)

| Geometrical Parameters | Methods | | | |
|---|---|---|---|---|
| | HF | B3LYP | | B3PW91 |
| | 6-311+G (d, p) | 6-31++G (d, p) | 6-311++G (d, p) | 6-311+G (d, p) |
| O8–C2–N9–H5 | 1.77 | 1.52 | 1.45 | 1.47 |
| N10–C2–N9–C1 | -0.87 | -0.33 | -0.33 | -0.29 |
| N10–C2–N9–H5 | -178.21 | -178.43 | -178.52 | -178.50 |
| O8–C2–N10–C3 | 179.86 | -179.98 | -179.89 | -179.88 |
| O8–C2–N10–H6 | 0.82 | 0.89 | 0.92 | 0.88 |
| N9–C2–N10–C3 | -0.17 | -0.02 | 0.08 | 0.08 |
| N9–C2–N10–H6 | -179.21 | -179.15 | -179.11 | -179.15 |
| N10–C3–C4–C1 | 1.95 | 2.06 | 2.01 | 2.02 |
| N10–C3–C4–N11 | -179.14 | -178.13 | -178.25 | -178.19 |
| C12–C3–C4–C1 | -178.48 | -178.44 | -178.33 | -178.30 |
| C12–C3–C4–N11 | 0.43 | 1.38 | 1.42 | 1.48 |
| C4–C3–N10–C2 | -0.43 | -0.86 | -0.94 | -0.97 |
| C4–C3–N10–H6 | 178.57 | 178.22 | 178.22 | 178.23 |
| C12–C3–N10–C2 | 179.95 | 179.59 | 179.36 | 179.33 |
| C12–C3–N10–H6 | -1.06 | -1.34 | -1.48 | -1.47 |
| C4–C3–C12–H13 | -142.54 | -153.09 | -148.54 | -148.84 |
| C4–C3–C12–H14 | -20.94 | -31.49 | -26.81 | -27.06 |
| C4–C3–C12–H15 | 98.57 | 86.99 | 91.96 | 91.62 |
| N10–C3–C12–H13 | 37.05 | 26.42 | 31.13 | 30.84 |
| N10–C3–C12–H14 | 158.65 | 148.03 | 152.86 | 152.62 |

$P_{21/a}$, space group configuration was clearly displayed. For the present case, except for some, all the atoms were arranged in a single plane which facilitates rigid formation of basis (pattern of atoms) on the lattice frame. From Figure 2, it was clear that all static lattice points were occupied by a set of hexagonal patterns which could be coupled with one another and form invariable molecular setup for amalgamating consistent orthorhombic crystal. There were some un-notified peaks with low intensity available similar to the activated peaks in the XRD modulated spectrum. They clearly showed the reciprocal lattice of the present crystal and also it illustrated other associated lattice formation in the organic composite.

In Figure 3, the molecular sequence has appeared over XYZ planes of crystal structure and 3D pattern in all planes clearly showed molecular configuration. In X plane, the molecular structure was found to be overlapped one another and the atoms on other plane were helped to couple nearby planes. In Y plane, it was seen that all the hexagonal frames were arranged diagonally in scattering mode where the planes are dispersed with respect to plane angle. In Z, plane, the molecular configuration was appeared to be arranged in vertically within the crystal planes. All the associated atoms were come into view out of the crystal planes where coupled atoms conjugated with nearby molecular elements of the subsequent plane have appeared. Thus, the characteristic condition $\alpha = \beta = \gamma = 90^{\circ}$ for orthorhombic lattice architecture was fulfilled. Such display clearly demonstrates $C_S$ point group of symmetry and thereby the $P2_12_12_1$ space group was assigned to that configuration. Therefore, from the above discussion, it was inferred that the orthorhombic crystal lattice was purposively organized non-centrosymmetric atomic planes in crystal and the NLO mechanism was mechanically facilitated.

### 4.2. Crystal profile

The as-prepared slap shaped crystal was measured to be 38 X 22 X 4.5 mm dimensions and one unit cell was contained 5 molecules. The space group was assigned as per the point group symmetry and its cell parameters are depicted in Table 1. The solid slab was possessed strong rigidity with consistent mechanical behavior. According to the cell dimension, the unit cell parameters were determined to be a = 4.75 Å, b = 7.10 Å, and c = 7.39 Å which emphasized the nature of orthorhombic lattice for the present organic composite crystal [3]. Such fluctuated cell dimensions were truly exhibited non-linear optical mechanism to induce optical birefringence effect.

The optical index measurement was carried out using two prisms setup with its bisector planes are arranged to make parallel to the principal dielectric planes. The dual prism system is restricted with one dielectric axis. Relatively for the present crystal composite, the refractive indices were measured as $n_1 = 1.586$, $n_2 = 1.963$, and $n_3 = 1.739$, respectively, and this measurement was made at $\lambda = 509$ nm. These values were computed on par with Sellmeier coefficients with respect to three principal dielectric axes and such values were supported by the literature [17]. For this case, the calculated birefringence ($\Delta n$) was determined to be 0.2106, was moderate to make fluctuated or modulated polarization optical light by means of double refraction and patterned pyrimidine hexagonal frame was one of the cause to generate double refraction effect. The Transparency range measured using the UV-Visible transmittance curve and it was ranged in the region of 409–1256 nm and it was detailed that, the present case was active beyond the UV region and it was extended up to IR region. This view of the present composite revealed the good optical characteristics over the visible region and if this material is used as the laser source it will be acting good source material for optical laser with a wide range of the visible regions. The Non-Linear optical coefficient is usually estimating the rate of SHG and then THG of the optical crystal and it was computed to be 7.82 pm/V which is comparatively high and the present composite was tend to generate good SHG and THG gradient. The damage threshold of the present composite was ranged at 10 ns from 1.08 to 3 GW/cm$^2$ and this is a good indication of crystal rigidity and found to be safe condition and high-quality air conservation.

### 4.3. Molecular/crystal parameters analysis

The molecular parameters are depicted in Table 2 for enabling the $P_{21}$ configuration for the present organic composite. The related lipophilicity and topological surface area is sketched in Figure 4. The Hydrogen bond donor and acceptor in molecule state the binding possibility of nearby molecules to form static intermolecular forces and thereby generate the static polarizability to help to take place variable dielectric path for getting through the light wave. Here they were calculated to be 2 & 4,

respectively, and saturated erratic dielectric polarization is possible. The rotatable bond was found to be 0 which will helpful for sustained molecular planes. The topological polar surface area of this case was 104 $A^2$ which is very a good indicator to make sufficient density inside the crystal. The heavy atom count was 12 and this is able to enable modulated molecular track for an optical wave to flow through. Number of the rotatable bonds was counted to be 1 which makes very useful for producing planar set up in the crystal formation. The molecular mass of the present molecule was 171.11 g/mol and this value was supporting good packing fraction for the crystal and this enables zero dislocation.

### 4.4. Molecular geometry profile

The optimized molecular geometry details are presented in Table 3 and the corresponding crystal view is presented in Figure 5. As the nitro and methyl injection in the Uracil frame, the structure was forcefully extended into multiple planes. Simultaneously, the entire configuration was altered and it is viable to facilitate various polarization indexes in the crystal. They were formally found in the bond length and bond angle variation and saturated distortion. The oxygen insertion in pyrimidine ring known as Uracil was pronounced in the bond lengths C1–O7 and C2–O8 as reduction of internuclear distance (1.208 and 1.209 Å). In addition, due to the alternative substitution of O, the C–N bond length differed by 0.020 Å. From this observation, it was clear that, by the application of heteronuclear bond influence on core ring, the chemical-equivalent forces come in effect to produce static polarizability and structure is able to produce dielectric atmosphere.

Besides, the coupling of nitro and methyl groups builds internuclear forces of attraction and repulsion among CC of the ring and thus, the alternation of bond length was signified in C2–N10 and C1–N9 as 1.399 Å and 1.409 Å. Similarly, the direct impact was known at C3–C4 and C1–C4 as 1.362 Å and 1.468 Å. Due to the repulsive forces existed on Os between $NO_2$ and = O of the ring. Here, two hydrogen acceptors and donors were present and for that, the interactive forces easily enabled between intra-

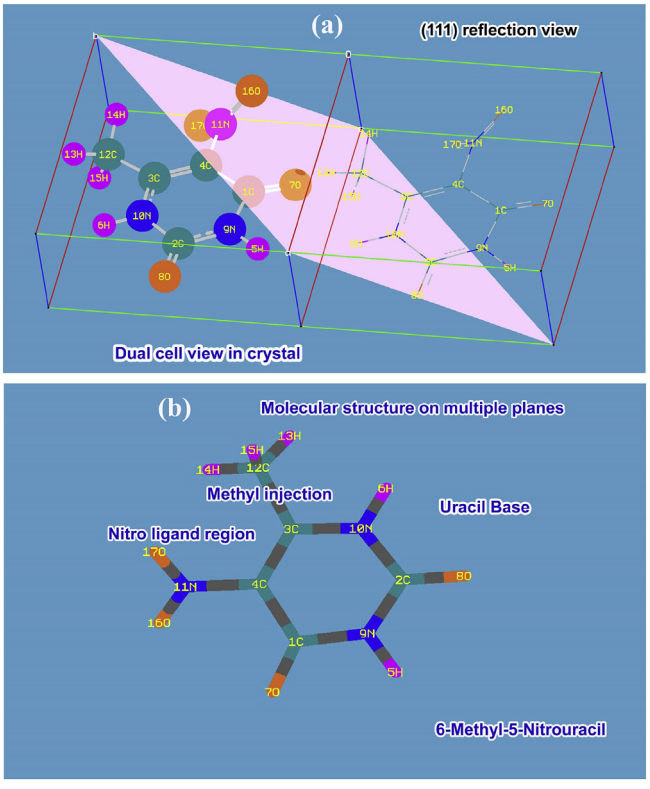


**Figure 5.** (a) Dual cell view (b) Tubular form of geometry of 6-methyl 5-nitro Uracil crystal.

molecular spaces. The substitutional effect also observed in the bond angle of semicircle C2–N10–C3 and C1–N9–C2 as nearly 125° and 128°, respectively. Unless, the substitutions on the ring, the bond angle on semicircle C1–C4–C3 was 120°. But it was more than the ring with ligand groups. Thus, all the bond parameters were coherent with the parameters of customized structure for providing good optical characteristics.

### 4.5. Molecular charge assignment analysis

Usually, after the formation of molecular orbital configuration assembly, the atomic charges are realigned with respect to molecular electrostatic forces of attraction and repulsion among molecular sites in intermolecular entities and it is denoted by color gradient which is ranged from green to red color of atoms. Two extreme color gradient showed electronic (electrophilic) and protonic (nucleophilic) region among the intra-molecular region. The chemic-operating potential for a rigid optical pathway can be easily identified among the core as well as allied molecular elements. The present molecule has specific charge dispersion characteristics and it was rated as a Mulliken charge measurement as in Figure 6.

Very strong heteronuclear bonds, weak hydrogen bonds, hybrid conjugated σ-σ* π-π* bonding system offered supra quantum spatial intermolecular hydrogen bond network which is expected to donate good crystal lattice amalgamation and comprehensive transparency for optical energy. Accordingly, here, two strong C=O heteronuclear bonds three C–N (imine) group bonds, two N–O, and the five C–H bonds were present. These bonds were created only by suitable charge orientation in the molecular site. Habitually, in this case, one core bond known as C3–C4 acted as the main source for inducing the local electric field for generating non-linear activity. Here, purposively, the molecular charges were about to be pushed up and pulled down in different molecular entities. As expected, in Uracil ring, the charges pulled away by = O groups whereas unexpectedly, charges pushed up to ring from NO group and C4 has taken negative charge effect to ignite the effective dipole moment in the core ring. Two extreme charge grids were connected together and sketch the Mulliken charge field and it is presented in Figure 5. These parallel charge grids were energetically linked the molecular planes in different modes of polarization and thereby three different pathways were created and thus optical waves were guided to make harmonically doubled.

### 4.6. Vibrational investigation

#### 4.6.1. Vibrational process assignment

The title compound has 17 atoms and thereby 45 normal and pure vibrational modes were assigned including 17 number of stretching, 14 number of in-plane and 14 number of out of plane bending modes. From the vibrational bands in both finger-print and group frequency regions, all are found to be pure and they are free from additional and subtraction bands. They are usually represented by A′ and A″ class of the vibrational modes and they are allocated as per the group theory on vibrational motion of the cyclic organic molecule. All signals from corresponding vibrations are verified with respect to the Gaussian hybrid method of calculations and they are observed on par with simulated spectra for both IR and Raman spectroscopic theory are presented in Figures 7 and 8 respectively. The calculated and experimental frequencies with intensity estimation are described in Table 4. Though the difference was observed between the characteristics frequencies of experimental and theoretical, the error termination calculations were made to coincide with one another.

#### 4.6.2. C–H vibrations

Since the core ring of the present case has no C–H bond, three C–H bonds derived from $CH_3$, all sets of vibrational modes should be observed in the spectral pattern. Accordingly, the C–H vibrational bands are observed with strong to medium intensity in the region 3000-2910 $cm^{-1}$ [18] for C–H stretching. Correspondingly, in-plane and out-of-plane

bending vibrations are forcefully allotted in the region 1250–910 and 900 - 710 $cm^{-1}$ respectively, [19, 20]. As per the expected limit, the C–H stretching signals have been found at 3000, 2990 & 2980 $cm^{-1}$, in-plane bending observed at 770, 730 & 670 $cm^{-1}$ and out of plane modes identified at 550, 540 & 460 $cm^{-1}$. Except for stretching bands, all bending vibrations were found to be moved down very much and this observation described that methyl group energy at the lower zone was consistently used for producing dipole moment with confined polarization magnitude (static bonds).

#### 4.6.3. N–H and C–N vibrations

The ring attached N–H bonds in pyrimidine ring is normally having enriched internuclear forces called force constant which tend to produce effective vibrations in the higher frequency regions. Accordingly, the N–H stretching vibrations of pyrimidine species are usually identified in the region 3400-3300 $cm^{-1}$ [21] and they are associated in-plane and out-of-plane bending modes for N–H are found in the region 1580–1510 and 1010-900 $cm^{-1}$ [22], respectively. Here, the N–H stretching modes were assigned with medium to a strong intensity at 3280 and 3270 $cm^{-1}$, in plane bending signals at 1610 and 1520 $cm^{-1}$ and out of plane modes at 1100 and 1050 $cm^{-1}$. The vibrational energy at the higher region was rather absorbed by the ring itself and such that, the stretching modes moved down to the lower region. This condition showed the energy at high frequency was utilized as dielectric energy. All bending modes were observed within and well above the expected limit which was mainly due to the low energy that was not transferred as chemical energy as well as dielectric energy.

Unless the present case was substituted by = O, the C=N bonds will be there. But due to such substitutions, C=N bond was converted into C–N bond. Such that the bond has a specific force constant with a high degree and due to which the identification of C–N vibrations in a normal vibrational patterns is not difficult. Therefore, the recognition of C–N stretching and bending modes is very easy to locate. As for previous work [22, 23, 24] is a concern, the C–N stretching is normally located in the region 1380-1266 $cm^{-1}$. In this title molecule, the bands were observed at 1450, 1430, 1400, and 1350 $cm^{-1}$ for C–N stretching. The above-observed frequency near at 1500 $cm^{-1}$ indirectly showed the imine bond (C=N) while frequency around 1300 $cm^{-1}$ designates the C–N. So, an energy related to bonds was almost the same and they proved strongly polarized dipoles. This is main the cause to come to conclude that, the molecule has strong plenty of dipoles in-unit topological surface area and thus it generates birefringence mechanism for extraordinary optical wave. The C–N in plane and out-of-plane bending group frequencies categorized as CNC and CCC at 400, 370 & 350, and 190, 160 & 140 $cm^{-1}$, respectively. These semicircle rings breathing on in-plane and out-of-plane were lowered down to well below-expected limit and these modes emphasize inelastic force constant and in that way, it proved its dipole mechanism to boost up the optical signal as an improved acute

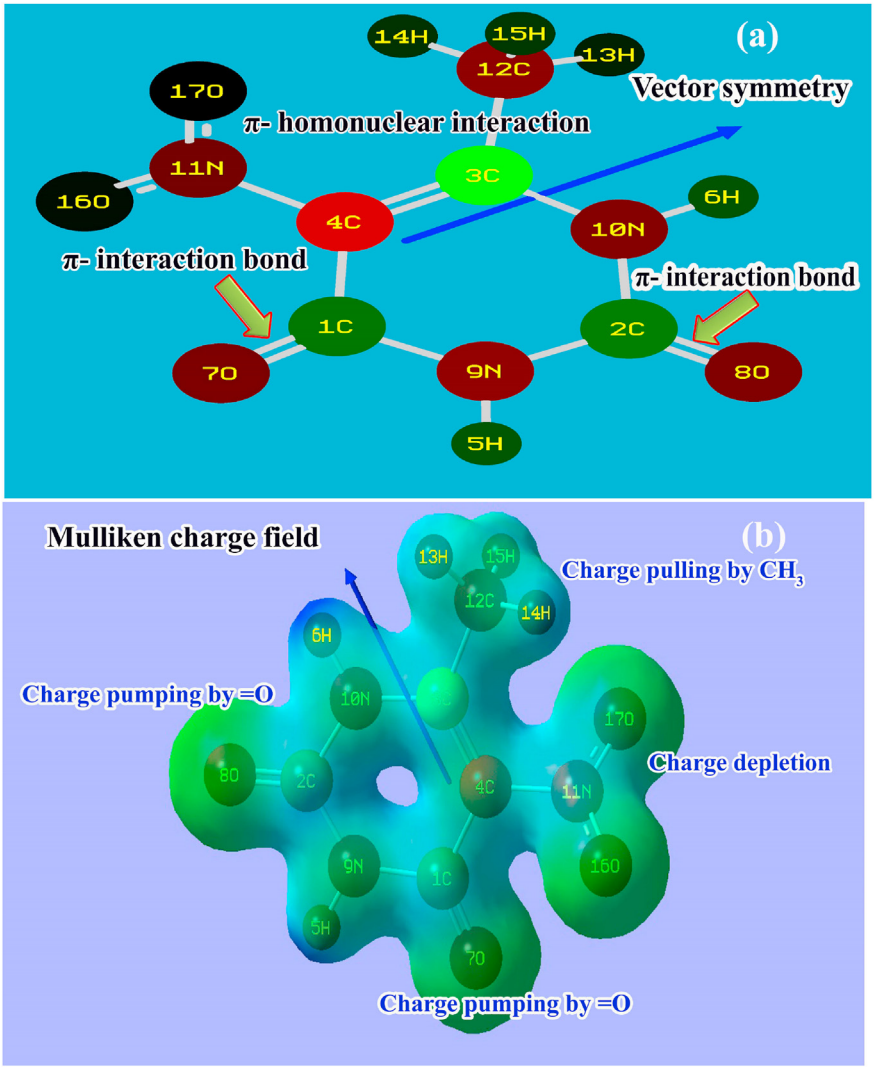


**Figure 6.** (a) open view (b) space points grid view of Mulliken charge distribution of 6-methyl 5-nitro Uracil crystal.

bi-angular acceptance in a noncollinear in the phase-control configuration.

#### 4.6.4. C=O vibrations

In the Uracil compound, the impact of the C=O bond is very high and play the important role in noncollinear phase-matching characteristics. As per the strong theory about the presence of a ketone group in α-pyridone, the C=O stretching vibration is present in the region 1690–1650 $cm^{-1}$ [25, 26]. For that reason, such a vibrational band was found with very strong intensity at 1720 and 1680 $cm^{-1}$ in the IR spectrum. Correspondingly, the in-plane and out-of-plane were observed at 980 & 860 and 310 & 206 $cm^{-1}$, respectively. All these vibrational observations strong inferred that, chemical-rigid and electrostatic mechanism is normally facilitated by C=O molecular strip on pyrimidine ring and it offered very fast frequency phase-matching optical amplification for producing femtosecond laser pulses [27, 28].

#### 4.6.5. $NO_2$ vibrations

Because of the nitro ligand group adoption on aromatic cyclic compounds, the base has specific spectral impression at the location of the group frequency region in IR and Raman spectra. All the fundamental vibrational modes for the nitro group are very much pronounced in their respective regions and the impact on other vibrations can be observed in the spectral model and they are rightly classified as stretching, in-plane, and out of plane bending. In the case of a nitro substituted compounds ortho-substituted with electron-donating group, the stretching is absorbed in the region 1515-1485 $cm^{-1}$ whereas those with electron-accepting groups absorb at 1570-1540 $cm^{-1}$. But, here, both groups were injected in ortho place and due to such pathetic situation, the stretching was observed at 1540 and 1460 $cm^{-1}$ [29, 30, 31] According to this condition, one was represented as asymmetric and other was symmetric and such vibrational energy in such region was not utilized whereas it forms preoccupied chemical energy to produce supportive static polarizability in a same plane as base compound. It helps to generate diverted optical boundary conduit for the flow of ordinary optical ray. Its in-plane and out-of-plane bending peaks observed for the same condition as above, in the region 865–830 and 590-500 $cm^{-1}$, respectively. As expected, in this case, in-plane bending was observed at 665 & 630 and 240 & 210 $cm^{-1}$ respectively. Due to the local static polarizability, low energy vibrations were found to be suppressed much.

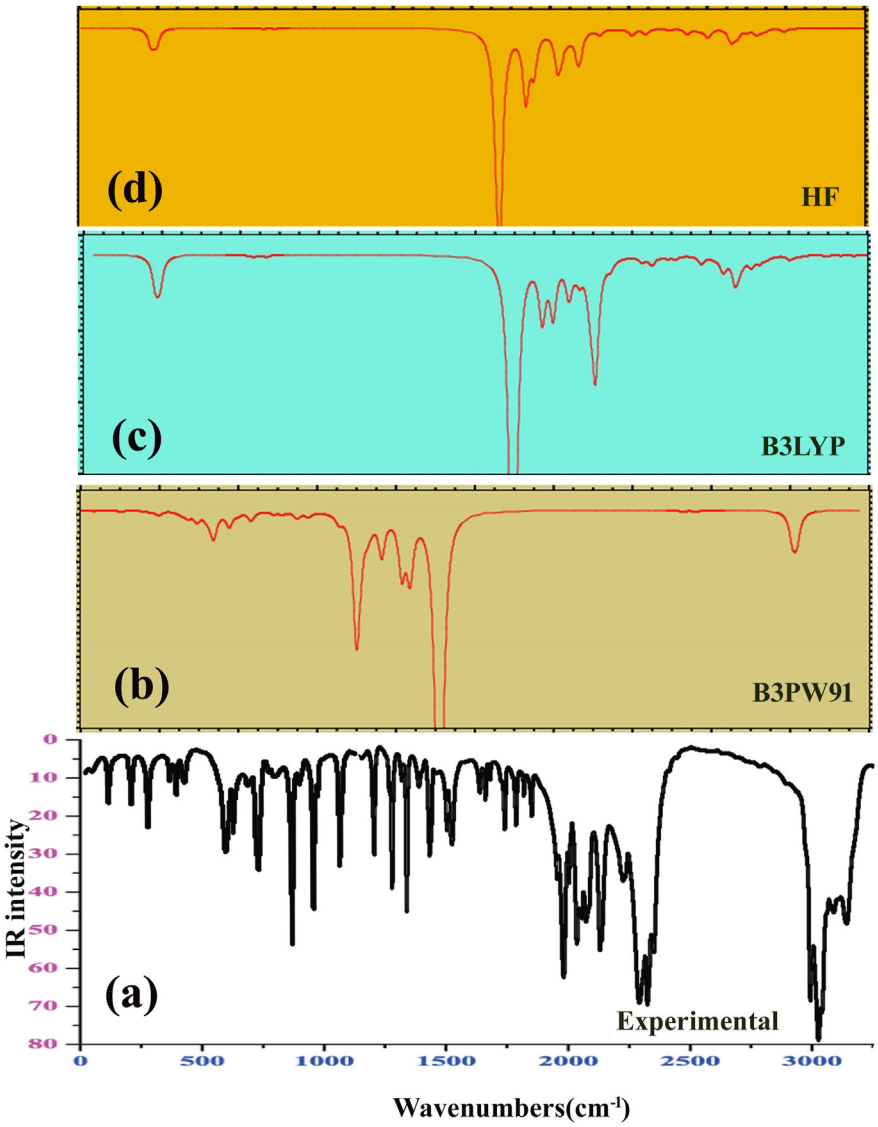


**Figure 7.** (a) Experimental (b) B3PW91 (c) B3LYP (d) HF model of FT-IR spectra of 6-methyl 5-nitro Uracil crystal.

### 4.7. NMR chemical analysis

For the present organic composite, the NMR resonance spectra were recorded and the parametric values are presented in Table 5 and the spectra are depicted in Figure 9. The NMR analytical results are always obtained by the means of chemical shift which is used to tracking the flow of chemical energy and oscillated chemical potential to identify the property as well as nodal zones residing of chemical-electric potential (a local electric field known as a dielectric boundary). Here, in this crystal material, the parallel Uracil frames making crystal configuration, according to the pyrimidine hexagonal ring, four core carbons and one allied carbon for methyl group were found in which four different ligand load were injected.

According to electronic dislocation, the chemical potential path is identified. Here, the ketone group was spotted at C1 and C2 by which the chemical shift of 186 and 187 ppm (Expt. 150 ppm) which are so high and also they showed lodging of equal chemical potential. External massive ligand such as methyl and nitro groups was injected by which the chemical shift of 192 and 138 ppm (Expt. 155 & 128 ppm) was observed. The higher chemical shift ensured the higher chemical energy pulling from the ring and low chemical shift explicit pushing of chemical potential to the ring. This view was clearly explained that the chemical parametric potential was exchanged between two ligand groups via ring and customize required chemical equivalent forces to retain stable dipole moment around the ring and simultaneously charge pumping was operated by the ketone group. This process sustained parallel in three different planes and different sets of the optical pathway with different diffusional mechanism were induced. The restored chemical energy in the form of an electric field was found on the core carbons which are to be circulated around the ring by ketone charge pumping and it is energized in three different ways and it is controlled by the exchange of chemical potential between nitro and methyl group. When the optical energy flows through such ring zones, it will be further energized by the above said mechanism and the frequency are doubled and even more than that it will be boosted additional and making third harmonic generation. From the chemical mechanism, it was inferred that the moderate THG can be achieved. If it is further improved, the structure should be adopted with some other electron-withdrawing group.

### 4.8. Molecular orbital interaction observation

The frontier molecular interaction on a molecule is usually drawn from the orbital energy grid points according to the spatial quantization and it is sketched in 3D form. The interactive orbitals are usually derived from electron cloud over entities of the molecule which are more interactive with respect to the degeneracy of orbitals. Such orbital interaction may be some times in phase and some times out of phase and the energy confinement on such orbitals mention the energy gap of the material. As

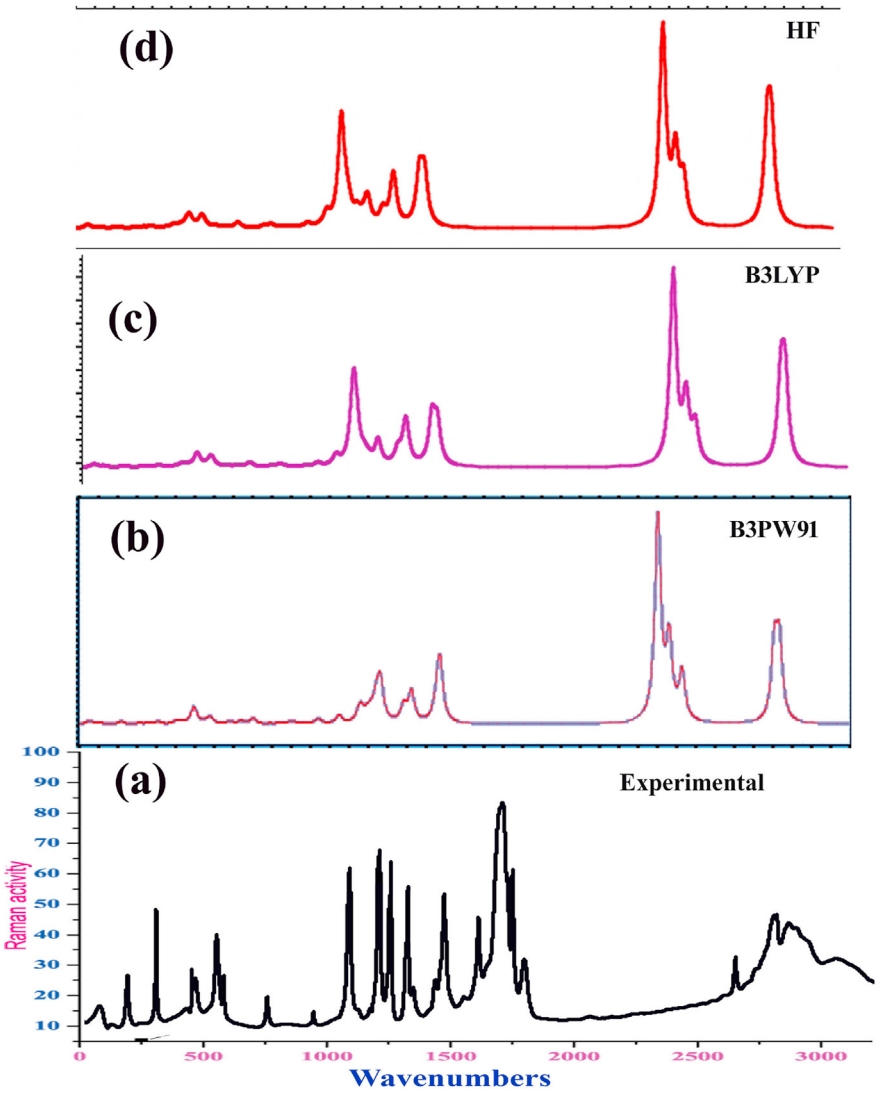


**Figure 8.** (a) Experimental (b) B3PW91 (c) B3LYP (d) HF model of FT-Raman spectra of 6-methyl 5-nitro Uracil crystal.

**Table 4.** Observed and calculated vibrational frequencies of 6-methyl 5-nitro Uracil.

| S. no. | Symmetry species $C_S$ | Observed frequency($cm^{-1}$) | | Methods | | | Vibrational Assignments & PED |
|---|---|---|---|---|---|---|---|
| | | | | HF | B3LYP | B3PW91 | |
| | | FT-IR | FT-Raman | 6-311++G (d,p) | 6-311++G (d,p) | 6-311++G (d,p) | |
| 1 | A′ | 3280m | - | 3162 | 3435 | 3447 | (N–H) **υ** (88%) |
| 2 | A′ | 3270vs | - | 3140 | 3415 | 3427 | (N–H) **υ** (75%) |
| 3 | A′ | 3000vs | 3000w | 3008 | 3003 | 3008 | (C–H) **υ** (80%) |
| 4 | A′ | 2990vs | 2990w | 2993 | 2998 | 2988 | (C–H) **υ** (72%) |
| 5 | A′ | 2980vs | 2990w | 2992 | 2970 | 2983 | (C–H) **υ** (78%) |
| 6 | A′ | 1720vs | 1720m | 1632 | 1723 | 1742 | (C=O)υ (71%) |
| 7 | A′ | 1680vs | 1680s | 1618 | 1698 | 1715 | (C=O)υ (69%) |
| 8 | A′ | 1610w | 1610s | 1502 | 1570 | 1587 | (N–H) **δ** (81%) |
| 9 | A′ | 1520m | 1520w | 1467 | 1518 | 1548 | (N–H) **δ** (78%) |
| 10 | A′ | 1510m | - | 1524 | 1442 | 1451 | (N–O)**υ** (73%) |
| 11 | A′ | - | 1460m | 1504 | 1414 | 1404 | (N–O)**υ** (76%) |
| 12 | A′ | 1450m | - | 1477 | 1391 | 1384 | (C–N)**υ** (81%) |
| 13 | A′ | 1430w | - | 1456 | 1671 | 1710 | (C–N)**υ** (80%) |
| 14 | A′ | 1400m | - | 1427 | 1336 | 1339 | (C–N)**υ** (65%) |
| 15 | A′ | 1350s | - | 1271 | 1330 | 1337 | (C–N)**υ** (60%) |
| 16 | A′ | 1280m | - | 1261 | 1313 | 1330 | (C–N)**υ** (66%) |
| 17 | A′ | - | 1200m | 1175 | 1241 | 1246 | (C=C)**υ** (80%) |
| 18 | A′ | - | 1180m | 1081 | 1147 | 1156 | (C–C)**υ** (80%) |
| 19 | A′ | 1150m | - | 1155 | 1348 | 1098 | (C–C)**υ** (78%) |
| 20 | A′ | 1100m | - | 1087 | 1289 | 1044 | (N–H) γ (68%) |
| 21 | A′ | - | 1050m | 1060 | 1000 | 1263 | (N–H) γ (78%) |
| 22 | A′ | 980w | 980m | 907 | 965 | 970 | (C=O) **δ** (73%) |
| 23 | A′ | 860m | - | 863 | 830 | 851 | (C=O) **δ** (67%) |
| 24 | A′ | 770m | - | 787 | 802 | 752 | (C–H) **δ** (77%) |
| 25 | A′ | 730w | - | 733 | 742 | 761 | (C–H) **δ** (90%) |
| 26 | A′ | 670s | - | 643 | 701 | 658 | (C–H) **δ** (87%) |
| 27 | A′ | 665s | - | 679 | 692 | 707 | (N–O) **δ** (91%) |
| 28 | A′ | 630w | - | 596 | 641 | 644 | (N–O) **δ** (68%) |
| 29 | A′ | 600m | - | 586 | 625 | 631 | (C–N) **δ** (58%) |
| 30 | A′ | 550m | - | 522 | 541 | 556 | (C–H) γ (59%) |
| 31 | A′ | 540m | 540w | 521 | 565 | 565 | (C–H) γ (61%) |
| 32 | A′ | - | 460w | 471 | 439 | 438 | (C–H) γ (68%) |
| 33 | A′ | - | 400w | 393 | 411 | 407 | (CNC) **δ** (58%) |
| 34 | A′ | 370m | - | 371 | 386 | 384 | (CNC) **δ** (66%) |
| 35 | A′ | 350w | - | 357 | 354 | 359 | (CCC) **δ** (78%) |
| 36 | A′ | 310w | - | 331 | 296 | 297 | (C=O) γ (76%) |
| 37 | A′ | 260w | - | 259 | 265 | 264 | (C=O) γ (73%) |
| 38 | A′ | - | 250w | 252 | 264 | 374 | (C–C) **δ** (74%) |
| 39 | A′ | 240w | - | 302 | 264 | 269 | (N–O) γ (58%) |
| 40 | A″ | - | 210w | 293 | 201 | 253 | (N–O) γ (48%) |
| 41 | A″ | 190w | - | 234 | 205 | 208 | (CNC) γ (48%) |
| 42 | A″ | 160w | - | 186 | 163 | 163 | (CNC) γ (58%) |
| 43 | A″ | 140w | - | 148 | 145 | 133 | (CCC) γ (53%) |
| 44 | A″ | 110w | - | 102 | 86 | 88 | (C=O) γ (52%) |
| 45 | A″ | - | 100w | 66 | 73 | 71 | (C=O) γ (61%) |

VS –Very strong; S – Strong; m- Medium; w – weak; as- Asymmetric; s – symmetric; υ – stretching; α –deformation, δ - In plane bending; γ-out plane bending; τ – Twisting.

the present case is the organic composite crystal, the in-phase and out of phase interaction is pronounced by the means of σ, π, and δ orbital coherence, and it are detailed in Figure 10. The chemical potential allocation on the material is nothing but the transition between electron domain acceptor and donor energy fascination facilitates the energy gap of crystal material and it is used to identify whether the crystal semiconductor or dielectric.

The set of donor orbitals knows as HOMO has electron affinity and another set of orbitals known as LUMO possessed ionization potential and those random transitions among such orbital domains enabled physico-chemical characteristics of the material. For the present case, the HOMO was represented by orbital lobe interaction that found on molecular orbitals of all molecular elements, except one N–H bond. The σ-bonding interaction was found in all HOMO domains and only one π-bonding segment that were observed in which the entire energy band was marked. In the case of HOMO-1, the electrons were found to be excited further and space orbital interaction moving away from atoms. Due to the excitation of electrons in second-order, all the σ-interaction

**Table 5.** Experimental and calculated $^{1}H$ and $^{13}C$ NMR chemical shifts (ppm) of 6-methyl 5-nitro Uracil.

| Atom position | TMS-B3LYP/6-311++G(2d,p) Shift (ppm) | | | Experimental shift (ppm) |
|---|---|---|---|---|
| | Gas | Solvent phase | | |
| | | DMSO | $CCl_4$ | |
| C1 | 186.47 | 186.41 | 184.22 | 150 |
| C2 | 187.41 | 187.38 | 186.04 | 150 |
| C3 | 192.83 | 192.71 | 188.16 | 155 |
| C4 | 138.53 | 138.48 | 136.67 | 128 |
| C12 | 20.04 | 20.01 | 18.86 | 28 |
| H5 | 7.17 | 7.17 | 7.02 | 9.7 |
| H6 | 6.37 | 6.36 | 5.89 | 3.3 |
| H13 | 1.16 | 1.15 | 0.96 | 1.7 |
| H14 | 7.91 | 7.92 | 8.22 | 9.8 |
| H15 | 1.47 | 1.46 | 1.29 | 2.0 |

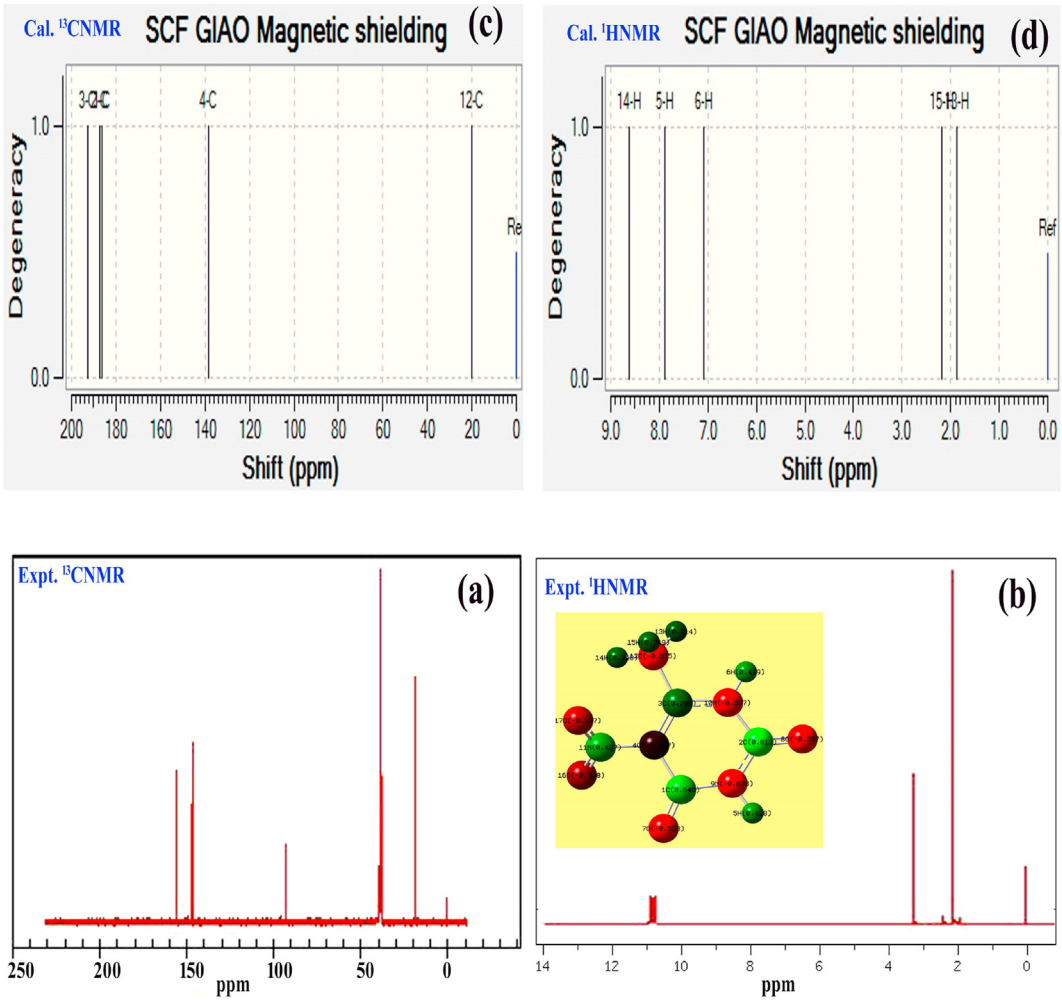


**Figure 9.** (a) Expt. CNMR (b) Expt. HNMR (c) Theor. CNMR (d) Theor. HNMR spectra of 6-methyl 5-nitro Uracil crystal.

orbitals were found to be blown from which it was infered that, orbital interaction process is varied from order to order.

In the case LUMO domain, hyperactive interaction taking place where σ-interaction and π-conjugation were dominated. The electron domain was found on C=O and methyl group, except those, all atoms were having empty zones to receive electrons with respective potential. The LUMO-1 is known as second-order empty zone where σ and π- interaction orbital system appeared and hence, the out of phase interaction has come in view. This view demonstrates energy of all orbitals is overlapped with one another and the energy on that domain is the same. Such type of discrete method of Uracil patterned HOMO and LUMO field proved the variable molecular arrangement in crystal and all sets of HOMO and

LUMO described the optical wave-guiding capability and dielectric mechanism for operating SHG. The Kubo gap was calculated from Table 6 and it was found to be 6.320 eV was so high and the present crystal was definitely the dielectric material and NLO active crystal.

### 4.9. UV-visible analysis/CT complex importance

The electronic absorption spectra provide important information regarding electronic energy and its related charge transfer complex (CT). It is a broad view of the distribution of vibrational energy of molecule and it is used to measure the chemical energy that is distributed among bonds of structure. The CT complex is the bond unit and is directly obtained from the molecular structure, it is identified from nodal points of chemical-electric potential and it is the pre-amalgamated main source to expose molecular property. For the present molecule come crystal, the UV-Visible spectra are depicted in Figure 11 and the observed values are portrayed in Table 7.

The observed electronic spectra were located in the spectral pattern at 401, 323, and 297 nm with the absorption energy gap of 3.0, 3.8, and 4.1 eV with oscillator strength of 0.007, 0.004 and 0.050, respectively, in the gas phase. The absorption peaks were characteristically assigned in n→σ* interactive orbital space zone and it was represented by Quartz UV along with the visible region. All the individual transitions were acknowledged in first-order and second-order energy provinces. The electronic absorption (H→L (63%)) was found to be started from UV region and thereby it was concluded that, the material will be active from UV to visible region along with IR. According to the orbital interactive region, the spectral energy in the electronic region was enormously used for producing material characteristics. The chemical energy consumption was invariably used to organize dielectric behavior in the present organic composite material. As per the selection rule of electronic spectra, the chemical energy of considerable amount was located in C=O, C=C and C–N bonds and therefore, the CT complex was identified to be C=O, C=C and C–N and energy of other bonds were supported the CT complex and these are the main motive for the molecular structure to be NLO active.

Similarly, the UV-Visible transmission spectra were observed in Figure 11 where different optical active regions were noted carefully. According to the Figure, the present case has wide UV-Visible activity and the optical transmission was observed from 400 nm which is starting point of visible region. The hyperactive optical activity was found to be enabled in a wide range of spectrum which clearly showed the material optically active in visible region as well as UV quartz region. Hence, optical transmission breakdown was recognized at 1000 nm which is beyond visible and this is related to IR. Thus, extensive nonlinear transmission regions were fanatically monitored over the range 50–1200 nm, simultaneously it was verified with a saturation curve with inversely

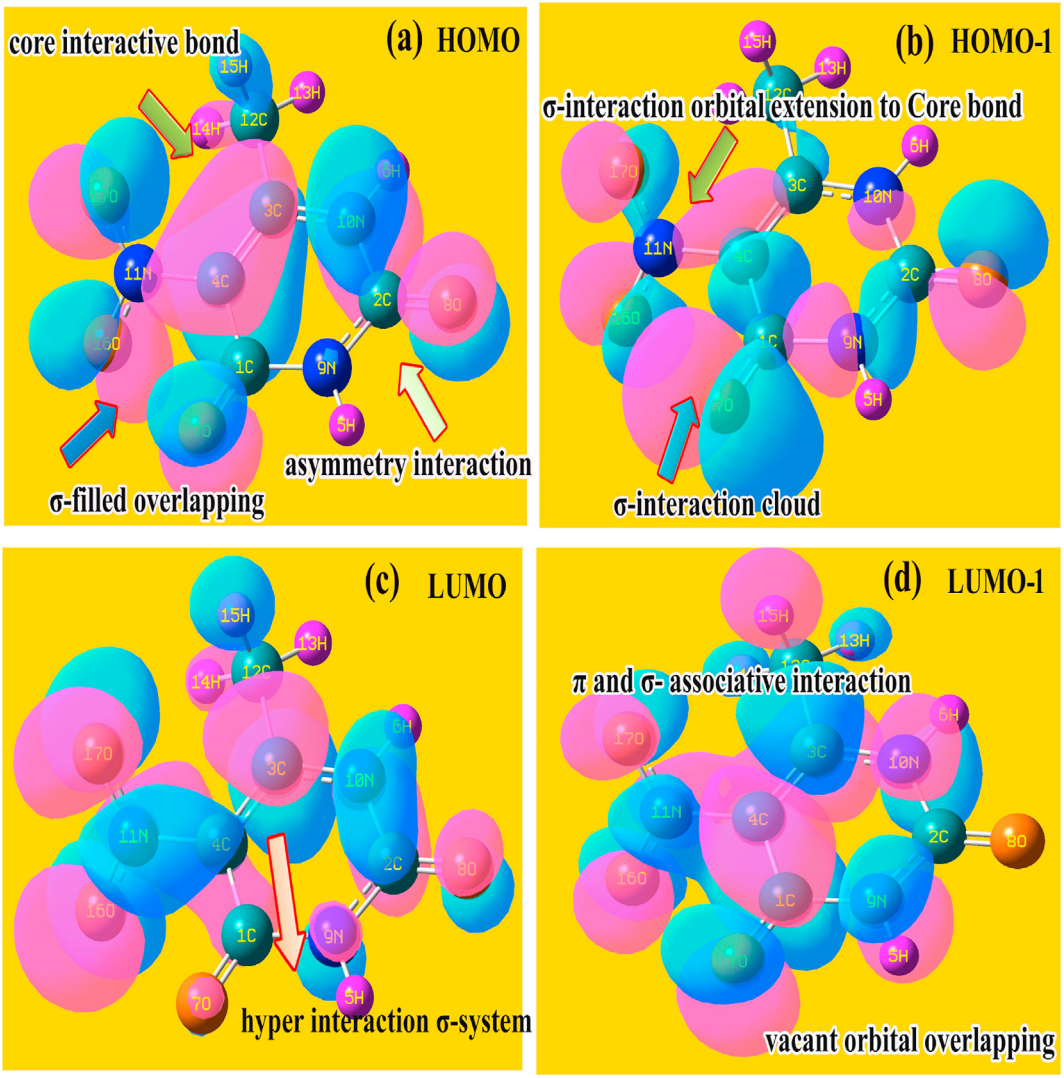


**Figure 10.** (a) HOMO (b)HOMO-1 (c) LUMO (d) LUMO-1 of 6-methyl 5-nitro Uracil.

proportional to the absorption and associated graded-index for refraction was measured to study the optical limiting. The laser activity is possible in this material and the efficiency was measured already in a crystal parameter study.

### 4.10. Physico-chemical property measurement

Usually, all physical parameters were calculated from molecular orbitals known as electron affinity and ionization potential. The zero-point energy is an important in profile that notifies the optimized structure and it was found to be 658.66 and 658.44 Hartree in IR and UV-Visible region respectively. These absolute magnitudes informed the right structure and it proved that, the crystal was having perfect molecular arrangements. The EA and IP were calculated to be 7.76 & 7.80 and 2.95 & 2.70 eV, respectively, and they differed which showed large bandgap assistance in the molecular structure and this confirms dielectric efficiency of the material. All the measured physico-chemical parameters are presented in Table 8.

The HOMO-LUMO energy gap was measured as 4.81 and 4.53 eV in IR and UV-Visible region respectively which showed the material efficiency and NLO active principle of the crystal [32, 33, 34, 35, 36]. The chemical hardness usually showed chemical stability to react with unwanted molecules and such that was found to be 2.40 and 2.26. From this observation, it was inferred that, hardness is moderate and contamination was not possible in this case. The chemical potential was calculated as 5.35 and 5.53 in both region and this value has not differed very much between the regions and that clearly illustrates that the molecule is edible to react with additive molecule to change or enhance the quality of the crystallinity. The electronegativity is usually reflecting the electronic domain density of the molecule and here, it was computed to be 5.35 and 5.53 in both region and it was concluded that the sufficient electronic domains were available to make parametric oscillation to facilitate crystal quality and chemical potential. The Electrophilicity index (ω) for this case was 3.15 and 3.17 which demonstrate electronic energy exchange among elements of the molecule and organizes resultant electronic property. The ECT of this case was +2.18 which obviously showed the electronic energy exchange from substitutions to ring structure in order to enhance the dielectric behavior and birefringence effect.

**Table 6.** Frontier molecular orbitals of 6-methyl 5-nitro uracil with energy levels.

| Energy levels | Frequency region B3LYP/6-311++G(d,p) (eV) | UV-Visible region (eV) |
|---|---|---|
| H+10 | 12.45302 | 11.96729 |
| H+9 | 12.22444 | 11.55722 |
| H+8 | 12.00865 | 11.51286 |
| H+7 | 10.687 | 10.37107 |
| H+6 | 9.282346 | 9.481805 |
| H+5 | 9.073635 | 9.322347 |
| H+4 | 8.996626 | 9.160983 |
| H+3 | 8.903836 | 8.73322 |
| H+2 | 8.717982 | 8.361241 |
| H+1 | 8.160965 | 8.241511 |
| H | 7.766672 | 7.800414 |
| L | 2.951618 | 3.270264 |
| L-1 | 2.030513 | 2.211197 |
| L-2 | 0.975528 | 1.489551 |
| L-3 | 0.763007 | 0.357013 |
| L-4 | 0.12354 | 0.265855 |
| L-5 | 0.041906 | 0.515656 |
| L-6 | 0.316468 | 0.635114 |
| L-7 | 0.523547 | 0.897703 |
| L-8 | 0.910221 | 1.050903 |
| L-9 | 1.134442 | 1.221247 |
| L-10 | 1.271316 | 1.412543 |

### 4.11. Dielectric configuration testing

The non-linear optical crystalline properties are usually extracted from the existence of dielectric axes of polarizability on different planes. The resultant and average polarizability of molecular entities provides the information on principal intermolecular electronic interaction on the noncritical behavior of hydrogen and heavy atoms network. All the homonuclear and heteronuclear molecular conjugative organic composite filled interstitial volumes of crystal and fulfill the high-quality crystal nature. Therefore the calculation on such polarizability and hyperpolarizability index on the dielectric axis is necessary to study the hyperactive NLO activity of the crystal [37, 38] and hence, for this case, the calculated parameters are presented in Table 9.

The first order polarizability was obtained in the dielectric axis $\alpha_{xx}$ known as I order Phase I, as 88.71 $\times$ $10^{-33}$ esu, at $\alpha_{yy}$ called as I order Phase II was found to be 68.65 $\times$ $10^{-33}$ esu and at $\alpha_{zz}$ referred as I order Phase III was observed to be 67.75 $\times$ $10^{-33}$ esu. All those effective electric polarizabilities of dielectric axes of crystal notified the strong summing of harmonic optical waves. The total and average polarizability on molecular configuration was measured to be 125.3 $\times$ $10^{-33}$ esu and 188 $\times$ $10^{-33}$ esu respectively for generating SHG phase-matching capability to assist SFG phase-matching configuration. The second-order hyperactive polarizability is known as hyperpolarizability on 3D dielectric axis and the hyperactivity was taking place some of the axes which showed very active axis to produce NLO activity. First activity was measured at $\beta_{xxx}$ pronounced as II order phase I to be 68.05 $\times$ $10^{-33}$ esu, the second was identified at $\beta_{xyy}$ as II order phase II to be 56.96 $\times$ $10^{-33}$ esu and the third was recognized at $\beta_{yyy}$ to be 73.63 $\times$ $10^{-33}$ esu. The total hyperactive measurement for all coordinates was observed to be 619.2 $\times$ $10^{-33}$ esu which showed the enrichment of second-order susceptibility of the material. Such values of non-linear coefficients fulfill the requirements for generating arbitrary harmonic generation with finite coefficients offered sum-frequency generation.

### 4.12. Electrostatic energy distribution analysis

The MEP filed was embedded by connecting electric flux grid points over the molecule in which the electrophilic and nucleophilic regions were clearly shown. The MEP gird potential was measured to be ±7.14 eV between electronegative and propositive zones around the molecule as in Figure 12. The electrophilic region has appeared over the molecular structure and it seemed to triangular configuration since O was found three places around the molecule. The nucleophilic zone was observed on N–H bonds and moderate zones were recognized over methyl groups and thus, the electrostatic potential was distributed on the molecular structure in the fluctuated approach. From this field allocation, it was confirmed that, the triangular attachment of core frames is possible to enable displacement of static dipole moment. The stationary intermolecular dielectric behavior illustrates the electric susceptibility and thereby such arrangement emphasizes high dense crystallinity. The distribution of the electric field was found as isosurface energy circulation which was to be very intense at O of the compound and it was suppressed over on N–H and methyl groups which notified high field expansion coefficient and such that helped to persuade dielectric inhibition.

### 4.13. NBMO energy transition examination

The electron domain exchange among non-bonding orbitals is inversely known as proton-transfer process in the homonuclear and heteronuclear bonding network ascribed transformation of chemi-equivalent potential to perform NLO active mechanism in the organic crystal. As pyrimidine was the main core and has stationary π and δ-bonding interaction complex in which the chemical energy is

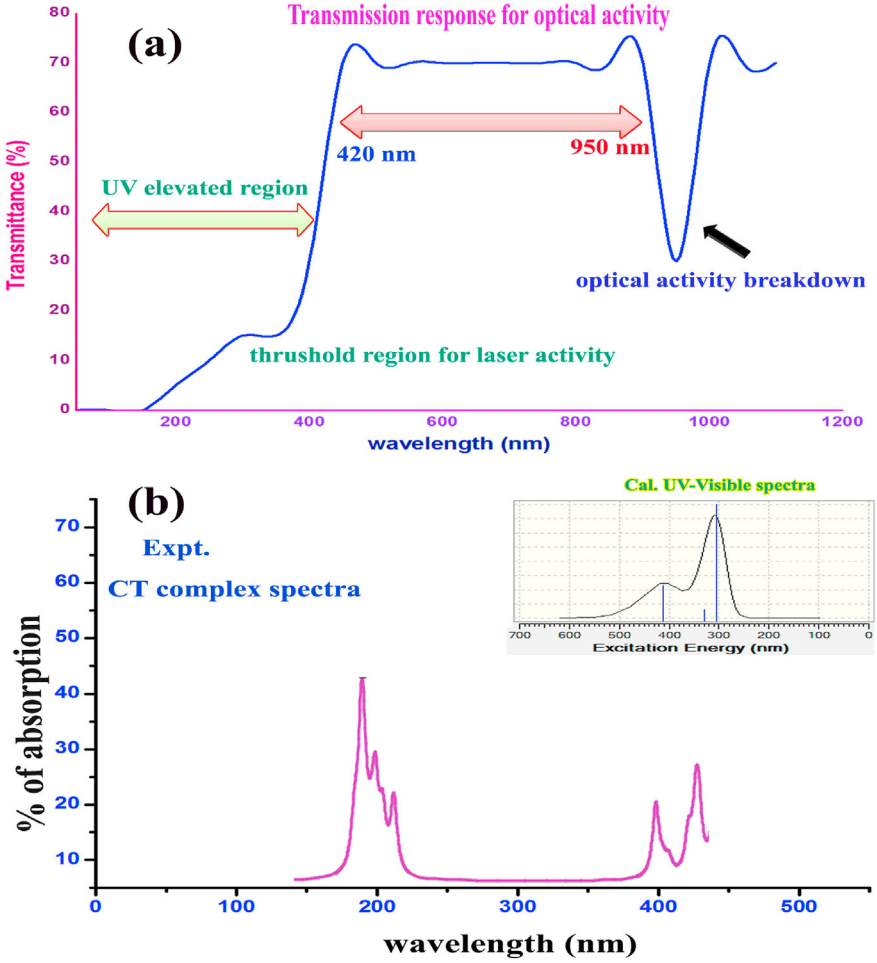


**Figure 11.** UV-Visible (a) Transmission (b) absorption spectra of 6-methyl 5-nitro Uracil crystal.

exchanged to fabricate possible way for optical waves to amplify the frequency of the intensive light wave. The entire energy is restored on some significant transitions and they are calculated as per the assigned energy of electronic orbitals which are portrayed in Table 10.

Usually, the transition is taking place between ground energy level and excited energy levels and the corresponding energy was assigned with respect to the bonding energy and restored chemical potential. Here, the first transition was found from C3–C4 to C1–O7, and N11–O16 by consumption of energy of 18.91 and 21.64 kcal/mol in π- π* bonding system. This exchange was represented by the ligand to ring energy flow. From the lone pair of O7 to C1 and C1–C4 by taking energy of 14.37 and 17.37 kcal/mol which was assigned on LP- N* complex system. Other transitions were observed from O8 to C2, C2–N9 and C2–N10 by the utilization of the energy of 16.07, 22.04 and 23.61 kcal/mol and the exchange process were assigned in LP- π* and LP- σ* orbital interaction systems. In nitro group, the transitions from N10 to C2–O8 and C3–C4 by

**Table 7.** Theoretical electronic absorption spectra of 6-methyl 5-nitro Uracil.

| λ (nm) | E (eV) | (*f*) | Transition level | Major contribution | Assignment | Region | Bands |
|---|---|---|---|---|---|---|---|
| Gas | | | | | | | |
| 401.85 | 3.0853 | 0.007 | H→L (63%) | H→L (63%) | n→σ* | Visible | R-band (German, radikalartig) |
| 323.42 | 3.8336 | 0.004 | H+2→L (61%) | H+2→L (61%) | n→σ* | Quartz UV | |
| 297.63 | 4.1657 | 0.050 | H+2→L-1(22%) | H→L-1(61%) | n→σ* | Quartz UV | |
| **DMSO** | | | | | | | |
| 402.12 | 3.0833 | 0.0007 | H→L (63%) | H→L (63%) | n→σ* | Visible | R-band (German, radikalartig) |
| 323.59 | 3.8316 | 0.0004 | H+2→L (62%) | H+2→L (62%) | n→σ* | Quartz UV | |
| 297.91 | 4.1618 | 0.0052 | H→L-1(61%) | H→L-1(61%) | n→σ* | Quartz UV | |
| **$CCl_4$** | | | | | | | |
| 411.34 | 3.0141 | 0.0006 | H→L (64%) | H→L (64%) | n→σ* | Visible | R-band (German, radikalartig) |
| 329.37 | 3.7643 | 0.0003 | H+1→L (48%) | H+1→L (48%) | n→σ* | Quartz UV | |
| 306.00 | 4.0517 | 0.0016 | H→L-1(60%) | H→L-1(60%) | n→σ* | Quartz UV | |

H: HOMO; L: LUMO.

**Table 8.** Calculated energies, chemical hardness, electro negativity, Chemical potential, Electrophilicity index of 6-methyl 5-nitro uracil in UV-Visible region.

| Parameter | B3LYP 6311++G (d,p) | UV-Visible | Electrophilicity charge transfer ($E_{CT}$) $(\Delta N_{max})_A$-$(\Delta N_{max})_B$ |
|---|---|---|---|
| $E_{total}$ (Hartree) | -658.6647 | -658.6494 | |
| $E_{HOMO}$ (eV) | 7.7667 | 7.8004 | |
| $E_{LUMO}$ (eV) | 2.9516 | 3.2703 | |
| $\Delta E_{HOMO\text{-}LUMO\ gap}$ (eV) | 4.8151 | 4.5301 | |
| $E_{HOMO+1}$ (eV) | 8.1610 | 8.2415 | |
| $E_{LUMO\text{-}1}$ (eV) | 2.0305 | 2.2112 | |
| $\Delta E_{HOMO+1\text{-}LUMO\text{-}1\ gap}$ (eV) | 6.1305 | 6.0303 | |
| Chemical hardness (η) | 2.4076 | 2.2651 | +2.18 |
| Electronegativity (χ) | 5.3592 | 5.5354 | |
| Chemical potential (μ) | 5.3592 | 5.5354 | |
| Chemical softness(S) | -9.6302 | -9.0602 | |
| Electrophilicity index (ω) | 3.1511 | 3.1772 | |
| Dipole moment | 5.7448 | 6.9378 | |
| ECT | 3.1511 | 3.1772 | |

absorbing the energy of 14.13 and 19.28 kcal/mol and entire energy system is known as LP- π* and LP- N*. Overturn, from O17 to C4–N11 and N11–O16 by taking the energy of 11.65 and 17.96 kcal/mol all the above transitions were prearranged on the NBMO system and they restricted by the strong hetero bonding interaction system. The most significant transitions were observed from O17 to N11–O16 and C3–C4 with the assigned energy of 136.79 and 79.35 kcal/mol from these observed transitional energies, it was clear that the huge amount of energy was exchanged between ring and nitro group with respect to the nonbonding domain. All the observed exchange energy confinement evidently proved the chemical potential amalgamation over different entities on molecular structure and thereby diverse polymorphic scattering nodal zones were present to enable the optical energy magnification.

### *4.14. VCD interpretation*

The vibrational circular dichroism pattern was visibly graphed in Figure 13 for the present organic crystal. Due to the $C_S$ point group of symmetry, the IR and Raman lines of the spectrum was obliviously displayed with adverse intensity and frequency sequence for all IR region was clearly noted as in the Figure. In far-IR region, as the intensity of peaks was very much low, they could not be predicted. But, the frequency in both transmission and absorption seemed to be in good order which expose the good homonuclear and hetero nuclear bond order and possessed superior scattering characteristics. As for as mid-IR is a concern, the peak intensity was so low and such sequential pattern revealed inactive bond order and they acted as an inactive center. In near-IR region, the signal intensity was so high when compared with other regions. Since, active bonds in that order were so active, the sequential Trans-absorb peaks were present. From all regions of the spectrum, the enantiomer character was well established in the present crystal which ensured the birefringence activity of the molecule.

## 5. Conclusion

In the present analysis, the molecular structure was examined to grow the crystal material; the deep investigation was made to interpret NLO generation mechanism. The crystal parameters were determined and discussed in detail. The XRD measurements ensured the non-centrosymmetric atomic planes present in crystal and that illustrates the operating condition of the organic complex NLO system. For this case, birefringence (Δn) was measured to be 0.2106, it was able to guide optical light. The optimized molecular parameters were evaluated and the direct change in bond parameters is discussed. The chemi-equivalent potential was identified from the storage of chemical energy and come in effect to produce static polarizability, thus produce dielectric susceptibility. The geometry profile of the molecule proved the stagnation of molecular planes for constructing diffusion mechanism for guiding the NLO waves. The vibrational analysis provides information concerning hydrogen and heavy atom bonding network to assist scattering ability to drive optical energy. The chemi-potential oscillatory motion of was determined by observing the chemical shift over the core carbons of the pyrimidine ring and retarding potential for operating NLO mechanism in the crystal geometry. Molecular cascading interaction on degenerate orbitals was monitored for identifying operating potential which is used for characterizing high-speed optical modulating light pulses. The wide range of nonlinear transmission was keenly observed from hyperactive

**Table 9.** Polarizability, Hyperpolarizability and Third-Harmonic-Generation Phase-Matching Configuration of 6-methyl 5-nitro Uracil.

| Parameter | a.u. | Parameter | a.u. |
|---|---|---|---|
| $\alpha_{xx}$ [I order Phase I] | -88.71 | $\beta_{xxx}$[II order phase I] | -68.05 |
| $\alpha_{xy}$ | -5.98 | $\beta_{xxy}$ | -7.41 |
| $\alpha_{yy}$ [I order Phase II] | -68.65 | $\beta_{xyy}$ [II order phase II] | 56.96 |
| $\alpha_{xz}$ | 0.633 | $\beta_{yyy}$ [II order phase III] | 73.63 |
| $\alpha_{yz}$ | 0.467 | $\beta_{xxz}$ | -8.22 |
| $\alpha_{zz}$ [I order Phase III] | -67.75 | $\beta_{xyz}$ | -2.11 |
| $\alpha_{tot}$ | 125.33 | $\beta_{yyz}$ | 5.96 |
| Δα | 188.07 | $\beta_{xzz}$ | -7.82 |
| $\mu_x$ | 2.15 | $\beta_{yzz}$ | -2.26 |
| $\mu_y$ | 4.42 | $\beta_{zzz}$ | 4.73 |
| $\mu_z$ | 0.290 | $\beta_{tot}$ | 619.28 |
| Δμ | 4.93 | | |

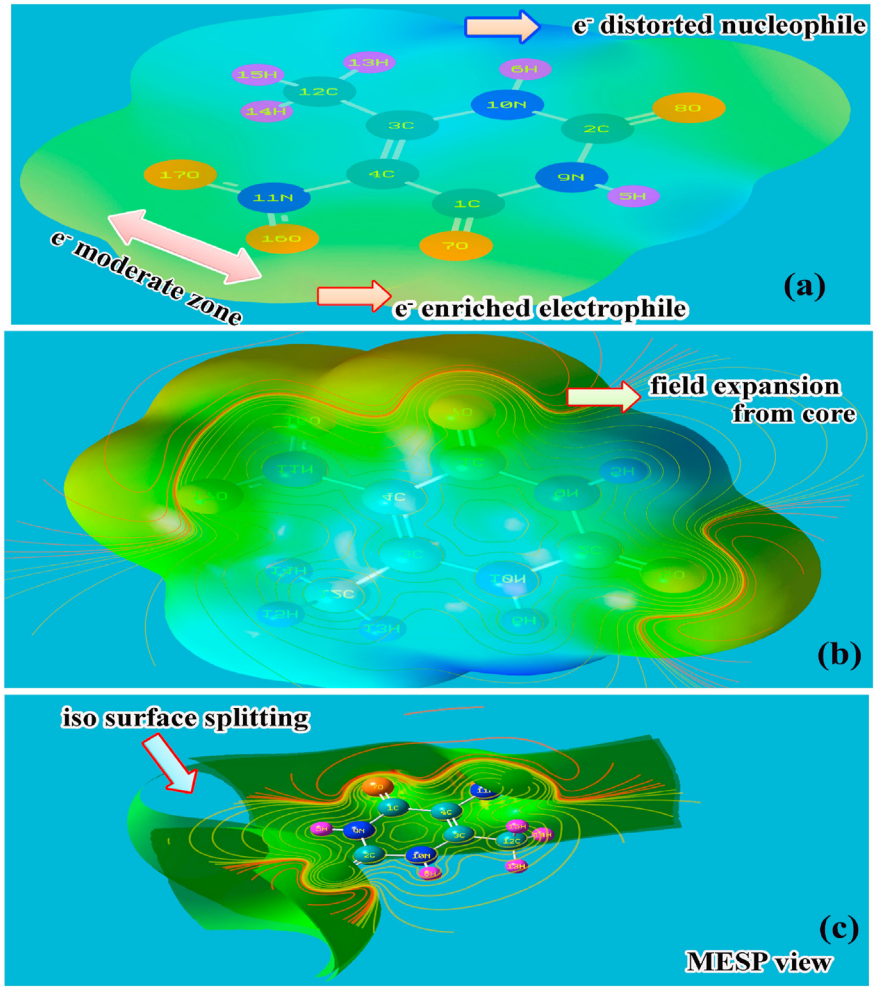


**Figure 12.** (a) space grid (b) Contour (c) isosurface view of MEP profile of 6-methyl 5-nitro Uracil crystal.

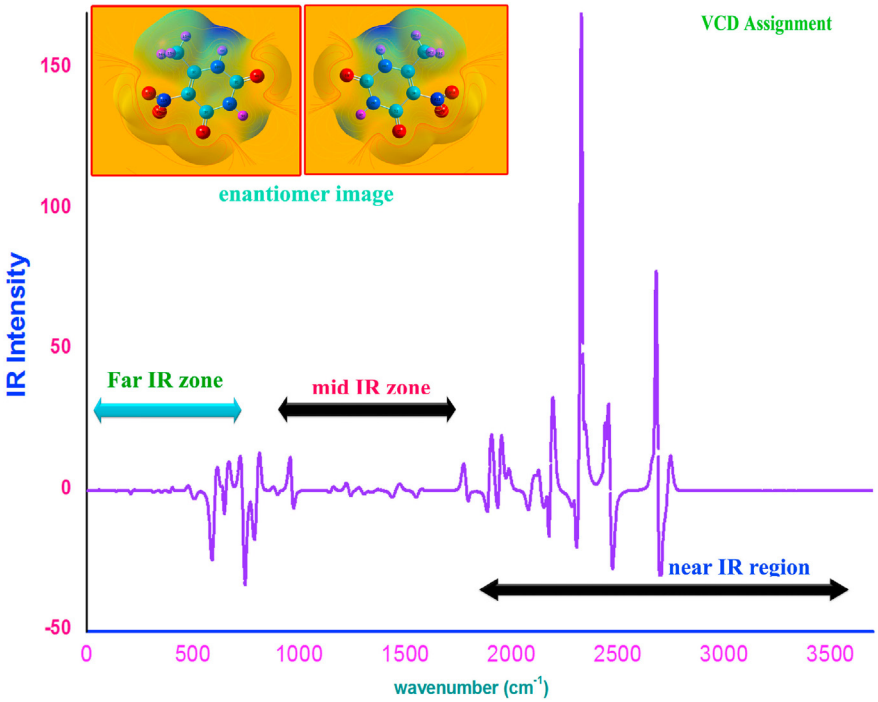


**Figure 13.** VCD spectra of 6-methyl 5-nitro Uracil crystal.

dielectric potential. The associated graded-index for refraction was measured from birefringence effect to study the optical limiting. The operating chemical potential restored in the main bonding system was distinguished from another bonding network of the molecular structure. The MEP field view was mapped and the field distribution on elements of molecular was studied. The enantiomer molecular set up was examined from peak intensity variation on different IR region and folding of molecular geometry on crystal lattice was analyzed by displaying VCD spectrum. In future, the organic composite will be tuned for enabling NLO efficiency as well as tuning will be made to enable monochromaticity in visible wavelength. Since the tuning is possible in laser activity for any wavelength of visible region; it can be made with material by adopting ligand template.

**Table 10.** The calculated NBO of 6-methyl 5-nitro uracil by second order Perturbation theory.

| Donor (i) | Type of bond | Occupancy | Acceptor (j) | Type of bond | E2 kcal/mol | Ej – Ei au | F(I j) au |
|---|---|---|---|---|---|---|---|
| **C1–O7** | π | 1.994 | **C3–C4** | π* | 4.67 | 0.37 | 0.039 |
| **C3–C4** | π | 1.804 | **C1–C4** | π* | 2.44 | 1.16 | 0.048 |
| **C3–C4** | π | | **C1–O7** | π* | 18.91 | 0.30 | 0.068 |
| **C3–C4** | π | | **C3–C4** | π* | 2.80 | 0.32 | 0.027 |
| **C3–C4** | π | | **N11–O16** | π* | 21.64 | 0.19 | 0.064 |
| **C3–C4** | π | | **C12–H15** | π* | 1.94 | 0.76 | 0.036 |
| **C3–N10** | σ | 1.979 | **C4–N11** | σ* | 3.40 | 1.04 | 0.054 |
| **C3–C12** | σ | 1.977 | **C4** | σ* | 2.07 | 1.76 | 0.054 |
| **C3–C12** | σ | | **C1–C4** | σ* | 4.50 | 1.00 | 0.060 |
| **C3–C12** | σ | | **C3–C4** | σ* | 2.22 | 1.23 | 0.047 |
| **C4–N11** | σ | 1.985 | **C3–N10** | σ* | 3.27 | 1.12 | 0.054 |
| **H5–N9** | σ | 1.969 | **C1–C4** | σ* | 2.63 | 1.02 | 0.047 |
| **H5–N9** | σ | | **C2–N10** | σ* | 4.13 | 0.94 | 0.056 |
| **H6–N10** | σ | 1.969 | **C2–N9** | σ* | 3.88 | 0.95 | 0.055 |
| **H6–N10** | σ | | **C3–C4** | σ* | 2.50 | 1.27 | 0.050 |
| **N11–O16** | σ | 1.995 | **C3–C4** | σ* | 4.72 | 0.44 | 0.043 |
| **N11–O16** | σ | | **N11–O16** | σ* | 7.65 | 0.31 | 0.052 |
| **C12–H13** | σ | 1.981 | **C3–C4** | σ* | 3.04 | 1.11 | 0.052 |
| **C12–H14** | σ | 1.970 | **C3–N10** | σ* | 4.74 | 0.81 | 0.055 |
| **C12–H15** | σ | 1.961 | **C3–C4** | σ* | 5.57 | 0.52 | 0.050 |
| **O7** | LP | 1.999 | **C1** | N* | 5.80 | 19.79 | 0.303 |
| **O8** | LP | 1.999 | **C2** | N* | 6.38 | 19.74 | 0.318 |
| **O16** | LP | 1.999 | **N11** | N* | 2.14 | 20.04 | 0.185 |
| **O17** | LP | | **N11** | N* | 2.99 | 20.05 | 0.219 |
| **O7** | LP | 1.999 | **C1** | N* | 14.37 | 1.64 | 0.137 |
| **O7** | LP | | **C1** | N* | 2.79 | 1.81 | 0.065 |
| **O7** | LP | | **C1–C4** | π* | 17.37 | 0.61 | 0.093 |
| **O7** | LP | | **C1–N9** | σ* | 24.53 | 0.56 | 0.106 |
| **O8** | LP | 1.978 | **C2** | N* | 16.07 | 1.59 | 0.143 |
| **O8** | LP | | **C2** | N* | 3.39 | 1.74 | 0.071 |
| **O8** | LP | | **C2–N9** | σ* | 22.04 | 0.55 | 0.100 |
| **O8** | LP | | **C2–N10** | σ* | 23.61 | 0.54 | 0.103 |
| **N9** | LP | 1.7461 | **C1–O7** | π* | 21.51 | 0.36 | 0.079 |
| **N9** | LP | | **C2–O8** | π* | 14.83 | 0.39 | 0.069 |
| **N10** | LP | 1.756 | **C2–O8** | π* | 14.13 | 0.40 | 0.068 |
| **N10** | LP | | **C3–C4** | π* | 19.28 | 0.38 | 0.077 |
| **O16** | LP | 1.983 | **N11** | N* | 4.41 | 1.91 | 0.082 |
| **O16** | LP | | **C4–N11** | σ* | 13.97 | 0.54 | 0.078 |
| **O16** | LP | | **N11–O17** | σ* | 17.47 | 0.69 | 0.099 |
| **O17** | LP | 1.973 | **N11** | N* | 5.11 | 1.90 | 0.088 |
| **O17** | LP | | **C4–N11** | σ* | 4.89 | 1.06 | 0.065 |
| **O17** | LP | | **C12–H14** | σ* | 5.03 | 1.26 | 0.071 |
| **O17** | LP | | **N11** | N* | 2.09 | 1.77 | 0.056 |
| **O17** | LP | | **C4–N11** | σ* | 11.65 | 0.56 | 0.072 |
| **O17** | LP | 1.973 | **N11–O16** | σ* | 17.96 | 0.71 | 0.102 |
| **O17** | LP | | **C12–H14** | σ* | 6.43 | 0.76 | 0.064 |
| **O17** | LP | | **N11** | N* | 3.14 | 2.36 | 0.088 |
| **O17** | LP | | **N11–O16** | σ* | 136.79 | 0.15 | 0.131 |
| **C1–O7** | π | 1.973 | **C3–C4** | π* | 79.35 | 0.01 | 0.061 |
| **C2–O8** | π | 0.043 | **C2–O8** | π* | 9.95 | 0.43 | 0.161 |
| **N11–O16** | σ | | **C3–C4** | π* | 12.11 | 0.13 | 0.055 |

## Declarations

### Author contribution statement

K. Sooryakala: Performed the experiments.

S. Ramalingam: Conceived and designed the experiments; Wrote the paper.

R. Maheswari: Contributed reagents, materials, analysis tools or data.

R. Aarthi: Analyzed and interpreted the data.

### Funding statement

This research did not receive any specific grant from funding agencies in the public, commercial, or not-for-profit sectors.

### Competing interest statement

The authors declare no conflict of interest.

### Additional information

No additional information is available for this paper.

## References

[1] G.R. Desiraju, Crystal Engineering: the Design of Organic Solids, Elsevier, Amsterdam,The Netherlands, 1989.
[2] G.R. Desiraju, Angew. Chem. Int. Ed. Engl. 34 (1995) 2311–2327.
[3] J. Jerphagnon, IEEE J. Quantum Electron. QE 7 (1971) 42–47.
[4] J.G. Bergman, J.R. Crane, Appl. Phys. Lett. 20 (1972) 21–28.
[5] Subhadip Roy, Antonio Bauza, Rupak Banik, Suresh Chandra Biswas, Antonio Frontera, Subrata Das, Tetrahedron 70 (2014) 6931–6937.
[6] V. Beaula Premavathi, S. Nelson Amirtharaj, S. Ramalingam, Adalya J. 8 (10) (2019) 1483–1511.
[7] Ch Venkata Reddy, I. Neelakanta Reddy, Kakarla Raghava Reddy, Shim Jaesool, Kisoo Yoo, Electrochim. Acta 317 (2019) 416–426.
[8] Nagappagari Lakshmana Reddy, Vempuluru Navakoteswara Rao, Murkinati Mamatha Kumari, Kakarla Raghava Reddy, Parnapalle Ravi, Marappan Sathish, Mani Karthik, Muthukonda Venkatakrishnan Shankar, Inamuddin, Chem. Lett. 16 (2018) 765–796.
[9] D. Kishore Kumara, Loskot Jan, Kříž Jan, Nick Bennett, Hari M. Upadhyaya, Veera Sadhu, Ch. Venkata Reddy, Kakarla Raghava Reddy, Sol. Energy 199 (2020) 570–574.
[10] Ch Venkata Redd, I. Neelakanta Reddy, K. Ravindranadh, Kakarla Raghava Reddy, Nagaraj P. Shetti, D. Kim, J. Shim, Tejraj M. Aminabhavi, J. Environ. Manag. 260 (2020) 1–9, 110088.
[11] P. NagarajShetti, Savio Dias, Kakarla Raghava Reddy, Nanostructured organic and inorganic materials for Li-ion batteries: a review, Mater. Sci. Semiconduct. Proces. 104 (2019) 104684, 1–9.
[12] Amit Mishra, Nagaraj P. Shetti, Soumen Basu, Kakarla Raghava Reddy, Tejraj M. Aminabhavi, ChemElectroChem 6 (2019) 5771–5786.
[13] Nagaraj P. Shetti, Deepti S. Nayak, Shweta J. Malode, Kakarla Raghava Reddy, Shyam S. Shukla, Tejraj M. Aminabhavi, Anal. Chim. Acta 1051 (2019) 58–72.
[14] Murat Cakici, Kakarla Raghava Reddy, Fernando Alonso-Marroquin, Chem. Eng. J. 309 (2017) 151–158.
[15] J.G. Bergman, G.R. Crane, B. F Levine, C.G. Bethea, Appl. Phys. Lett. 20 (1972) 21–23.
[16] B.M. Pierce, R.M. Wing, In molecular and polymeric OptoelectroniMc aterials: fundamentalsa nd applications, Proc. Soc. Photo Opt. Instrum. Eng. 682 (1986) 27–36.
[17] Youping He, Genbo Su, Bochang Wu, Rihong Jang, J. Cryst. Growth 119 (1992) 393–398.
[18] Socrates George, Infrared and Raman Characteristic Group Frequencies (Tables and Charts), John Wiley & Sons, Ltd, 2001.
[19] Y. Xue, D. Xu, D. Xie, G. Yan, Spectrochim. Acta Part A 56 (2000) 1929–1938.
[20] Y. Xue, D. Xie, G. Yan, Int. J. Quant. Chem. 76 (6) (2000) 686–699.
[21] J. Fabian, Bulletin de la Societe Chimique de France 5 (1956) 1499–1506.
[22] S. Ramalingam, S. Periandy, S. Mohan, Spectrochim. Acta Part A 77 (2010) 73–81.
[23] Paul M. Smith, Mario F. Borunda, Adv. Condens. Matter Phys. 3296845 (2017) 1–7.
[24] M. Silverstein, F.X. Webster, Spectrometric Identification of Organic Compounds, sixth ed., John willey, Asia, 2003.
[25] L.J. Bellamy, The Infrared Spectra of Complex Molecules, Chapman and Hall, London, 1975.
[26] J. Kavalıirova, M. Korabik, P. Stachova, J. Moncol, R. Sillanpa, T. Lis, D. Miklos, M. Melnık, J. Mrozinski, D. Valigura, Polyhedron 27 (2008) 1333–1342.
[27] S.X. Dou, D. Josse, J. Zyss, J. Opt. Soc. Am. B 8 (1991) 1732–1739.
[28] S.X. Dou, D. Josse, R. Hierle, J. Zyss, J. Opt. Soc. Am. B 9 (5) (1992) 687–697.
[29] C.J.W. Brooks, J.F. Monnan, J. Chem. Soc. (1961) 3372–3379.
[30] F. Todd Simmons Richard, Kenneth Love, L. Kreuz, J. Org. Chem. 31 (7) (1966) 2400–2401.
[31] Adam Allerh, Paul von R. Schleyer, J. Am. Chem. Soc. 85 (4) (1963) 371–380.
[32] Ch Venkata Reddy, I. Neelakanta Reddy, Bhargav Akkinepally, Kakarla Raghava Reddy, Jaesool Shim 814 (2020) 1–8, 152349.
[33] V. Navakoteswara Rao, N. Lakshmana Reddy, M. Mamatha Kumari, P. Ravi, M. Sathish, K.M. Kuruvilla, V. Preethi, Kakarla Raghava Reddy, Nagaraj P. Shetti, Tejraj M. Aminabhavi, M.V. Shankar, Appl. Catal. B Environ. 254 (2019) 174–185.
[34] Chandragiri VenkataReddy, I. NeelakantaReddy, V.V.N. Harish, Kakarla Raghava Reddy, Shim Jaesool, Ceram. Int. 45 (2019) 15298–15306.
[35] Ravindranadh Koutavarapu, Bathula Babu, Ch Venkata Reddy, I. Neelakanta Reddy, Jaesool Shim, 265, (2020), 110504, 1-9.
[36] Shivaraj B. Patil, Patil S. Basavarajappa, Nagaraju Ganganagappa, M.S. Jyothi, A.V. Raghu, Kakarla Raghava Reddy, Int. J. Hydrogen Energy 44 (2019) 13022–13039.
[37] Dongfeng Xue, Siyuan Zhang, J. Solid State Chem. 142 (1) (1999) 156–162.
[38] B.M. Pierce, R.M. Wing, Proc. Soc. Photo Opt. Instrum. Eng. 682 (1986) 27–32.